Hydrous Phase Relations and Trace Element Partitioning Behaviour in Calcareous Sediments at Subduction-Zone Conditions

Susanne Skora[1,2]*, Jon D. Blundy[1], Richard A. Brooker[1], Eleanor C. R. Green[2], Jan C. M. de Hoog[3] and James A. D. Connolly[2]

[1]School of Earth Sciences, University of Bristol, Wills Memorial Building, Queen's Road, Bristol BS8 1RJ, UK, [2]Institute of Geochemistry and Petrology, Earth Sciences, ETH Zurich, Clausiusstrasse 25NW, 8092 Zurich, Switzerland and [3]Edinburgh Ion-microprobe Facility, School of Geosciences, University of Edinburgh, Kings Buildings, West Mains Road, Edinburgh EH9 3JW, UK

*Corresponding author. E-mail: Susanne.Skora@erdw.ethz.ch

ABSTRACT

We report the results of experiments on two natural marine sediments with different carbonate contents (calcareous clay: $CO_2 = 6.1$ wt %; marl: $CO_2 = 16.2$ wt %) at subduction-zone conditions (3 GPa, 750–1200°C). Water (7–15 wt %) was added to the starting materials to simulate the effects of external water addition from within the subducting slab. The onset of melting is at 760°C in water-rich experiments; melt becomes abundant by 800°C. In contrast, the onset of melting in published, water-poor experiments occurs at variable temperatures with the production of significant melt fractions being restricted to more than 900°C (phengite-out). The different solidus temperatures ($T_{solidus}$) can be ascribed to variable fluid X_{H2O} [$H_2O/(CO_2 + H_2O)$], which, in turn, depends on bulk K_2O, H_2O and CO_2. Partial melts in equilibrium with residual garnet, carbonate, quartz/coesite, epidote, rutile, kyanite, phengite, and clinopyroxene are granitic in composition, with substantial dissolved volatiles. Supersolidus runs always contain both silicate melt and solute-rich fluid, indicating that experimental conditions lie below the second critical endpoint in the granite–H_2O–CO_2 system. Carbonatite melt coexists with silicate melt and solute-rich fluid above 1100°C in the marl. The persistence of carbonate to high temperature, in equilibrium with CO_2-rich hydrous melts, provides a mechanism to both supply CO_2 to arc magmas and recycle carbon into the deep Earth. The trace element compositions of the experimental glasses constrain the potential contribution of calcareous sediment to arc magmas. The presence of residual epidote and carbonate confers different trace element characteristics when compared with the trace element signal of Ca-poor marine sediments (e.g. pelagic clays). Notably, epidote retains Th and light rare earth elements, such that some melts derived from calcareous sediments have elevated Ba/Th and U/Th, and low La/Sm$_{PUM}$, thereby resembling fluids conventionally ascribed to altered oceanic crust. Our results emphasize the importance of residual mineralogy, rather than source lithology, in controlling the trace element characteristics of slab-derived fluids.

Key words: experimental petrology; subduction; carbon-bearing sediment; CO_2 solubility; carbon recycling

INTRODUCTION

The carbon cycle has important consequences for a wide variety of geological processes, including planetary accretion, climate change, diamond formation, carbonatite volcanism and mantle metasomatism (e.g. Javoy *et al.*, 1982; Marty & Jambon, 1987; Caldeira, 1992; Franck *et al.*, 1999; Sleep & Zahnle, 2001; Hayes & Waldbauer, 2006; Dasgupta & Hisrchmann, 2010;

Rohrbach & Schmidt, 2011; Walter et al., 2011; Hazen et al., 2012; Dasgupta, 2013). Subduction zones provide the major geotectonic settings in which crustal carbon can penetrate deep into the Earth's interior, or return to the surface via arc volcanism. Carbon itself can occur in several species and in various lithologies in the subducted crust; for example, organic matter and methane in sediments (e.g. Suess & Whiticar, 1989; Nishio et al., 1998), hydrothermal calcite in the upper oceanic crust (e.g. Alt et al., 1986; Staudigel et al., 1989; Alt & Teagle, 1999), or biogenic carbonate-bearing sediments (e.g. Rea & Ruff, 1996; Plank & Langmuir, 1998). At present, subduction of substantial amounts of sedimentary carbonate is limited to relatively few convergent margins (Vanuatu, Sunda, Central America, Lesser Antilles) and therefore altered oceanic crust is considered the main carrier for carbon in most subduction zones (e.g. Dasgupta & Hisrchmann, 2010). Where carbonate sediments are known to subduct, they impart a distinct carbon isotopic signal (e.g. Sano & Marty, 1995; Sano & Williams, 1996; Van Soest et al., 1998; Shaw et al., 2003; de Leeuw et al., 2007).

Carbon-rich sediments undergo devolatilization and melting during subduction, providing a mechanism for returning some of their carbon inventory back to the exosphere. A key question is what proportion of the carbon is released by such processes and returned to the surface and what proportion is carried in the slab to mantle depths. This question is ultimately linked to the stability and solubility of the different carbon species along subduction-zone geotherms. Because carbonates are stable to high temperature and are relatively insoluble in aqueous fluids, carbon that is subducted in the form of carbonate is likely to be largely retained in the slab beyond sub-arc depths (e.g. Yaxley & Green, 1994; Kerrick & Connolly, 1998; Molina & Poli, 2000; Kerrick & Connolly, 2001a, 2001b; Poli et al., 2009). Likewise an assemblage of pure carbonate minerals would be unlikely to melt at sub-arc conditions, owing to their relatively high solidus temperatures at these pressures (1100–1300°C, Irving & Wyllie, 1975). Based on thermodynamic models, Kerrick & Connolly (2001b) proposed that the bulk of the subducted carbon inventory is transferred as solid carbonate to greater mantle depths and plays a relatively minor role in arc magmatism. These calculations were performed for a closed system; that is, in the absence of externally derived H_2O-rich fluids and associated melting. Kerrick & Connolly acknowledged that the infiltration of H_2O-rich fluids would promote sub-arc decarbonation of marine sediments. However, in subsequent open-system models of slab decarbonation it was found that substantial amounts of carbonate persisted beyond sub-arc depths despite infiltration (Connolly, 2005).

Other experimental studies on calcite solubility suggest that carbon could potentially be mobilized in more complex fluids that contain other elements, such as dissolved NaCl (e.g. Manning et al., 2013). Another route for transporting CO_2 back to the Earth's surface is via silicate partial melts from the subducted slab. These could potentially dissolve much greater quantities of CO_2 (or other carbon species) compared with subsolidus fluids. However, experimental phase equilibria studies on hydrous calcareous sediment (e.g. Thomsen & Schmidt, 2008a, 2008b; Tsuno & Dasgupta, 2012; Tsuno et al., 2012) suggest that these lithologies are essentially refractory under 'normal' subduction-zone conditions, specifically slab-top temperatures of $800 \pm 50°C$ at 2·5–4·5 GPa (e.g. Van Keken et al., 2002; Syracuse et al., 2010; Cooper et al., 2012). Thus, CO_2 in sediments is again surprisingly resistant to remobilization during subduction at sub-arc and shallower depth.

The apparent resistance of carbonates to participation in subduction-zone melt generation disagrees with the observation that many arc magmas contain appreciable CO_2, possibly in quantities even higher than those recorded by melt inclusions in volcanic phenocrysts (Blundy et al., 2010). The challenge is then to explain the substantial CO_2 flux from volcanic arcs (e.g. Burton et al., 2013) in the light of the apparent refractory behaviour of subducted carbonates. Following Kerrick & Connolly (2001b) and Gorman et al. (2006) we venture that externally derived H_2O plays a key role. Most previous experiments on calcareous sediments were performed either dry (Tsuno & Dasgupta, 2011) or by adding negligible water in excess of that stored in hydrous minerals (Thomsen & Schmidt, 2008a, 2008b; Tsuno & Dasgupta, 2012; Tsuno et al., 2012; Mann & Schmidt (in press)). Here we test the hypothesis that the addition of appreciable excess water ('flush melting'; e.g. Poli & Schmidt, 2002) from underlying lithologies enhances melting of subducted carbonate-bearing rocks, as suggested previously for carbon-free sediments (e.g. Hermann & Spandler, 2008; Skora & Blundy, 2010). A good candidate for providing such external water at sub-arc depths is serpentine (Ulmer & Trommsdorff, 1995), although other hydrous minerals may also contribute (e.g. lawsonite, zoisite, etc.; e.g. Schmidt & Poli, 1998; Van Keken et al., 2011; Spandler & Pirard, 2013).

METHODS

Starting materials

Samples were taken from the Lesser Antilles arc in the West Indies because it is a subduction zone in which the subducting sediments are a mixture of continental detritus and marls with varying proportions of clay and carbonate (e.g. Carpentier et al., 2008). We selected two different sediments from Deep Sea Drilling Project (DSDP) Leg 14 (Hayes et al. 1972), such that one (144A-3-1W 79-80: referred to as 144-16 or 'HC' hereafter) would be representative of the average of subducting marls in terms of carbonate/clay (CaO/SiO_2) ratio (Fig. 1), whereas the other (144-8-3W 130-135: called 144-38 or 'LC' hereafter) would be chemically close to some previously studied calcareous sediments. Sample 144-16 (HC) is from Unit 2, and consists of finely and densely mottled marls with around 30–65% carbonate
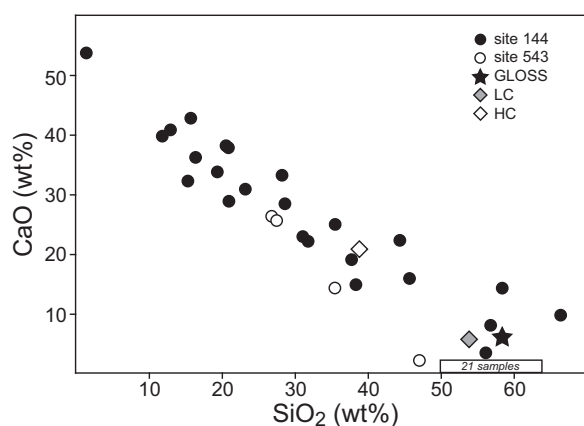
Fig. 1. Variation of CaO vs SiO_2 (wt %) for subducting sediments in the Lesser Antilles (circles) that are a mixture of continental detritus and marls with varying proportions of clay to carbonate. Experimental starting materials (diamonds) were selected such that one (HC) is representative of the average of subducting marls, whereas the other (LC) is chemically close to some previously studied compositions (see text). Sediment data are from Carpentier *et al.* (2008); GLOSS (star) is from Plank & Langmuir (1998). The box labelled '21 samples' indicates the number of natural samples that plot into that narrow compositional range.

Table 1: Starting compositions

Sample:	144-16	144-38	GLOSS	GLOSS 1σ
wt %				
SiO_2	38·8	53·8	58·6	2·5
TiO_2	0·38	0·81	0·62	0·04
Al_2O_3	9·64	13·8	11·9	0·9
Fe_2O_3	3·28	3·26	—	—
FeO	0·10	3·76	5·21	0·42
MnO	0·07	0·10	0·32	0·13
MgO	1·33	2·26	2·48	0·16
CaO	20·8	5·62	5·95	1·75
Na_2O	2·04	1·31	2·43	0·2
K_2O	1·66	2·21	2·04	0·16
P_2O_5	0·09	0·14	0·19	0·05
H_2O	6·5	7·8	7·29	0·41
CO_2	16·2	6·1	3·01	1·44
Sum	100·8	100·9	100·0	3·6

XRF data for 144-16 and 144-38 are from Carpentier *et al.* (2008). Fe^{2+}/Fe^{3+}, CO_2 and H_2O estimates are from this study. GLOSS is from Plank & Langmuir (1998).

component (foraminifera, coccoliths, triturated fragments). This unit is rich in zeolites (5–15%), and contains trace radiolarians and some pyrite. Sample 144-38 (LC) is from Unit 5, the bottom part of core 8, described as quartzose calcareous mudstone to calcareous clay, comprising clay minerals and organic matter, significant quantities of quartz and pyrite, ~10% carbonate (shell fragments, foraminifera) and trace mica. Although it was not our intention to conduct experiments on a global aggregate bulk composition (see Hermann & Spandler, 2008) it is worth noting that for major elements, except Na_2O and FeO^{tot}, LC lies within 2σ of GLOSS (Plank & Langmuir, 1998) (Table 1).

The rock powders used for this study are splits from the same samples as studied by Carpentier *et al.* (2008,

2009), who reported major (Table 1), and trace element and isotopic compositions. In Table 2 the sediment compositions are compared, on an anhydrous basis, with the experimentally studied compositions of Thomsen & Schmidt (2008*a*, 2008*b*), Tsuno & Dasgupta (2011, 2012), Tsuno *et al.* (2012) and Mann & Schmidt (in press). Additional experimental work on calcareous sediments, but at higher pressures ($\geq$5 GPa: Domanik & Holloway, 2000; Grassi & Schmidt, 2011*a*, 2011*b*; Tsuno *et al.*, 2012) will not be discussed here. To further verify the chemistries of our starting materials we fused a diluted version of both samples, consisting of 80 wt % albite and 20 wt % calcareous sediment. Measured and recalculated concentrations agree to within ±2% for major and ±4% for minor elements compared with the values of Carpentier *et al.* (2008).

Because Carpentier *et al.* (2008) reported only loss on ignition values for the sediments, we measured the bulk C contents and ferric/ferrous ratios of the sediments. The HC and LC lithologies have a total carbon content of 16·2 and 6·1 wt % respectively. Assuming that only H_2O and CO_2 are lost on ignition, initial H_2O contents are 6·5 and 7·8 wt % respectively. Sample HC is unusually rich in ferric iron, with $Fe^{3+}/Fe^{tot} = 0·97$. Sample LC has Fe^{3+}/Fe^{tot} of 0·46, which is comparable with altered oceanic crust (e.g. Dungan *et al.*, 1979). The significance of the Fe^{3+}-rich bulk-rock compositions for the experimental run products, as well as for extrapolation of the results to nature, is discussed below. We also tried to estimate the bulk sulphur contents by quantifying SO_3^{2-} in the diluted glasses by electron microprobe analysis (EMPA). Unfortunately, concentrations were below detection by EMPA, despite prolonged counting times. A conservative estimate of the detection limit for sulphur is 300 ppm for our analytical conditions, which suggests that the sulphur content of both compositions did not exceed 1500 ppm if dilution is taken into account, although it cannot be excluded that some sulphur was lost during fusion. In any case, Connolly & Cesare (1993) and Prouteau & Scaillet (2013) suggested that sulphur would significantly alter the phase relations only if it occurs in wt % quantities.

Lastly, we acknowledge that we have chosen to work with real sediments, despite the knowledge that any subducted lithology may be chemically modified during prograde metamorphism and devolatilization. Unfortunately, the magnitude of any such chemical modification is poorly constrained, and can vary on a local scale. Nevertheless, all subducted crustal lithologies have in common that most of their structurally bound water is lost during prograde metamorphism (e.g. Schmidt & Poli, 1998; Van Keken *et al.*, 2011). Water may be reintroduced at sub-arc depths; for example, by dehydration of underlying serpentinites (Ulmer & Trommsdorff, 1995)—a scenario that is simulated here. The loss of CO_2 during initial subduction to about 80 km should be insignificant for all but the hottest subduction-zone geotherms (Kerrick & Connolly, 2001*a*; Gorman *et al.*, 2006). Elements that are most

Table 2: Starting compositions of this and other studies (volatile-free; normalized to 100%)

Study: Sample:	TS 144-16	TS 144-38	T&S08a AM	T&S08b Bulk MC	T&D11 HPLC1	T&D12 HPLC2	Tetal12 HPLC3/4	M&Sp MP3	M&Sp MP3a
Majors (wt %)									
SiO_2	49·6	61·5	50·4	54·5	63·8	63·8	57·5	66·3	64·0
TiO_2	0·48	0·93	—	—	0·65	0·66	0·7	0·67	0·72
Al_2O_3	12·3	15·8	24·2	23·1	13·3	13·2	16·1	15	16·6
FeO^{tot}	4·35	8·51	9·75	—	6·48	6·48	7·8	6·86	6·86
MnO	0·09	0·11	—	—	0·18	0·18	0·2	—	—
MgO	1·70	2·58	2·12	7·8	2·61	2·62	3·1	2·31	2·37
CaO	26·6	6·43	7·20	12·5	8·52	8·52	10·2	5·60	5·76
Na_2O	2·61	1·50	2·54	—	2·38	2·37	2·3	1·25	1·49
K_2O	2·12	2·53	3·81	2·06	2·10	2·10	2·1	2·02	2·26
P_2O_5	0·11	0·16	—	—	—	—	—	—	—
Sum	100	100	100	100	100	100	100	100	100
Mg#	0·41	0·35	0·28	—	0·42	0·42	0·42	0·38	0·38
CaO/SiO_2	0·54	0·10	0·14	0·23	0·13	0·13	0·18	0·08	0·09
bulk CO_2	16·2	6·1	4·8	2·1	5·0	5·0	5	4·0	4·0
bulk H_2O	20–23	7·8–24	1·1	3·6	—	1·0	0·5/1·0	1·1	0·65
K_2O/H_2O	0·1	0·1–0·3	3·5	0·6	—	2·1	4·2/2·1	1·8	3·5
H_2O/CO_2	1·2–1·4	1·3–3·9	0·2	1·7	—	0·2	0·1/0·2	0·3	0·2

T&S08a,b, Thomsen & Schmidt (2008*a*, 2008*b*); T&D11, Tsuno & Dasgupta (2011); T&D12, Tsuno & Dasgupta (2012); Tetal12, Tsuno *et al.* (2012); M&Sp = Mann & Schmidt (in press).

susceptible to loss via fore-arc devolatilization, such as N, B, Cs, As and Sb (e.g. Bebout *et al.*, 1999), are not the focus of this study. The behaviour of other trace elements [e.g. large ion lithophile elements, high field strength elements, rare earth elements (REE)] is complex, and it has been suggested that they may be lost (e.g. John *et al.*, 2004), redistributed (e.g. Spandler *et al.*, 2003), or enriched in newly crystallized accessory phases (e.g. Sorensen *et al.*, 1997) during metamorphism and accompanying fluid–rock interactions. In the absence of a consensus, our experiments provide first-order estimates of the relative mobilities of trace elements. Most importantly, the natural starting materials were used without any additional trace element inventory. We have previously shown (Skora & Blundy, 2010, 2012) that doping starting materials with trace elements can lead to results that are difficult to extrapolate to nature.

Experimental and analytical methods

Bulk carbon analyses of the starting materials were obtained using a LECO CHN-900 at the Mikrolabor, Department for Organic Chemistry at ETH Zürich. Duplicate analyses of *c.* 2 mg of both bulk compositions indicate a precision better than 0·5 wt %. Ferric/ferrous ratios were determined at the FRX laboratory at the University of Lausanne. The chemical dissolution procedure largely follows the method detailed by Wilson (1960), and the FeO (wt %) content is determined colorimetrically. The concentration of ferric iron is calculated from the measured FeO and the bulk-rock (X-ray fluorescence; XRF) total Fe data given by Carpentier *et al.* (2008).

Powdered, hydrous starting material was loaded together with *c.* 7–15 wt % distilled water into Au (750–900°C) and $Au_{80}Pd_{20}$ (1000–1200°C) capsules, which were then welded shut (final H_2O content

≈15–22 wt %, Table 3). Experimental procedures are similar to those reported by Skora & Blundy (2010). Experiments were carried out in a ½ inch, end-loaded piston-cylinder at the University of Bristol at 3 GPa pressure and temperatures from 800 to 1200°C. Experiments were quenched by turning off the power; cooling to below 100°C occurred in <10 s. The pressure cell consisted of inner spacers of crushable alumina, a graphite furnace, and an outer sleeve of salt and Pyrex, requiring a friction correction of 3% (McDade *et al.*, 2002). Each experimental run contained one LC and one HC charge, run on top of each other. Some repeat experiments were run with a single charge. To keep temperature gradients to a minimum we compressed each of the capsules such that their combined lengths were between 5 and 8 mm. We also produced glasses of the bulk starting material from mixtures of 80% albite and 20% calcareous sediment melted at 1350°C and 1·5 GPa for 2 h in $Au_{80}Pd_{20}$. The high dilution rates were necessary so that the high volatile contents of the sediments could be fully homogenized and quenched to vesicle-free glass.

The LC 800°C experiment was repeated at ETH Zürich after two Bristol runs seemed to have experienced significant chemical zoning as a result of the large water contents used. Details of these runs are given in Supplementary Data file SD 1 (supplementary data are available for downloading at http://www.petrology.oxfordjournals.org). At ETH, the rocking multi-anvil was used in piston cylinder mode. This apparatus is designed to reduce chemical segregation in fluid-rich high-pressure experiments (Schmidt & Ulmer, 2004). The piston cylinder was rocking continuously during heating and pressurizing, and the rocking rate was then changed to a 15 min cycle for the remaining run time. Pressure cells consisted of MgO fillers, a graphite furnace, and an outer sleeve of talc and Pyrex, requiring a friction correction of 10% (McDade *et al.*,

Table 3: Run conditions and phase proportions ($P = 3\,GPa$)

Run	Time	T	H_2O	Major phases (%)								Fish	Accessories, others
		(°C)	(wt %)	cpx	grt	SiO_2	phen	ky	carb	ep	glass*	eggs	
Carbonate-rich lithology													
144-16-c1†	6 days	800	23	20	—	22	18	—	25	8	7	no	rt
144-16-c3†	4 days	850	23	17	—	16	15	—	24	10	18	no	rt
144-16-c6	3 days	900	25	‡	—	trace	—	—	25	17	58	no	rt
144-16-c7	1·5 days	1000	23	—	6	—	—	—	19	—	75	yes	
144-16-c14	1·5 days	1000	20	—	10	—	—	—	22	—	68	yes	
144-16-c18	19 h	1100	23	—	—	—	—	—	6	—	94	yes	carbonatite
144-16-c16	6 h	1200	23	—	—	—	—	—	0	—	100	yes	carbonatite
Carbonate-poor lithology													
144-38-c35$	8 days	750	7·8	15	23	31	27	trace	4	trace	—	yes	rt, apa, Fe-s
144-38-c34†$	10 days	750	16	—	31	29	23	1	3	trace	13	yes	rt, apa, Fe-s
144-38-c28$	6 days	800	7·8	—	28	15	6	3	4	trace	43	no	rt, apa, Fe-s
144-38-c29$	6 days	800	15	—	30	7	—	2	3	trace	57	no	rt, apa, Fe-s
144-38-c4	4 days	850	21	—	31	trace	trace	1	2	trace	66	yes	ilm, rt
144-38-c15	4 days	850	23	—	32	trace	trace	1	2	trace	65	yes	ilm, rt
144-38-c11	3 days	900	22	—	34	trace	—	1	trace	—	65	yes	ilm, rt
144-38-c13	1·5 days	1000	22	—	23	—	—	—	—	—	77	yes	rt
144-38-c19	19 h	1100	24	—	—	—	—	—	—	—	100	yes	

Mass balances (MB) were performed using anhydrous compositions. cpx, clinoproxene; grt, garnet; SiO_2, quartz/coesite; phen, phengite; ky, kyanite; carb, carbonate; ep, epidote; rt, rutile; ilm, hematite-rich ilmenite; apa, apatite; Fe-s, Fe-sulphide.

*Individual proportions of carbonatite and silicate glass could not be estimated by mass balance because silicate glass pools where never sufficiently large to be free of contamination by tiny carbonatite spherules.

†MB adjusted based on visual estimates.

‡MB suggests that some cpx should still be present in this run, providing a host for missing Na_2O, FeO, MgO, etc.

$Experiments repeated at ETH Zürich using the rocking piston cylinder; less water was used in these.

2002). Two capsules with reduced water contents of 7·8 wt % (structurally bound water only) and 15 wt % were run on top of each other for the 800°C experiment. We also performed two single-charge experiments at 750°C (7·8 and 15 wt % H_2O). Temperature gradients were calculated for the ETH experiments using the approach detailed by Hernlund *et al.* (2006), as they are critical to constraining the solidus temperature (Table 3). Results suggest that the two capsules run on top of each other at 800°C experienced the largest temperature variation (800–822°C) because of their 9 mm total length. The single-capsule, 750°C experiments with 7·8 and 15 wt % H_2O, respectively, experienced lesser temperature variation (749–758°C and 749–761°C, respectively).

No attempt was made to control or monitor fO_2 during the experiments. Thus oxygen fugacity could be controlled either by the initial bulk Fe^{2+}/Fe^{3+} (e.g. Kägi *et al.*, 2005), or by the intrinsic fO_2 of the furnace assembly (e.g. Truckenbrodt *et al.*, 1997). Starting compositions have moderate (LC) to high (HC) ferric/ferrous ratios, as discussed above. Unpublished estimates of the intrinsic fO_2 of the Bristol piston cylinder apparatus, using alumina–salt–Pyrex assemblies, lie 2 ± 1 log units above the nickel–nickel oxide (NNO) buffer. In either case, the experimental run products should record relatively oxidized conditions, which is consistent with experimental charges that contain rare quench anhydrite, hematite-rich ilmenite, and epidote. The intrinsic fO_2 of the ETH piston cylinder apparatus, using magnesia–talc–Pyrex assemblies, is unknown but the presence of Fe-sulphide instead of quench anhydrite suggests somewhat more reduced conditions below $NNO + 1$

(e.g. Prouteau & Scaillet, 2013). In any case, the systematic variations imply that the furnace assembly does exert a certain control on the fO_2, although it is not clear whether complete equilibration is always achieved. We can further estimate a minimum Fe^{2+} content for all experiments in which the majority of the bulk iron is contained in silicates with known (calculated) Fe^{2+}/Fe^{3+} contents, such as garnet, clinopyroxene, carbonate and phengite ($T = 750$–900°C). At $T > 900$°C more than 30% of the bulk iron is contained in the melt phase, which can have variable Fe^{2+}/Fe^{3+} (e.g. Stamper *et al.*, 2014). The calculations suggest that significant reduction has occurred in LC experiments conducted at ETH (subsolidus: 97%; suprasolidus: $\sim$92–95% Fe^{2+min}) as well as in Bristol ($\sim$87–90% Fe^{2+min}). We show below that these slight remaining differences in Fe^{2+}/Fe^{3+} result in insignificant differences in the LC phase assemblages (presence or absence of some hematite-rich ilmenite, more or less Fe_2O_3 in rutile). Calculated Fe^{2+min} values are less precise owing to mass-balance problems for the HC experiments, although they appear to be significantly lower ($\sim$35–70% Fe^{2+min}). We argue below that our HC phase relations are probably relevant only to high fO_2 conditions in natural environments.

Polished run products were investigated petrographically and geochemically using SEM (Universities of Lausanne and Bristol), EMPA (University of Lausanne and ETH Zürich), and the NERC ion-microprobe (University of Edinburgh). Detailed analytical protocols have been given by Skora & Blundy (2010). Silicate glasses were analyzed for their trace element content using a Cameca ims4f ion-microprobe using the analytical protocol of Skora & Blundy (2010, 2012); that is,

negative $^{16}O^-$ ions, 14·5 kV primary beam, 4·5 kV secondary beam, 3–5 nA sample current, ∼15–20 μm spot size and 75 ± 20 eV energy filter. For reasons given by Skora & Blundy (2012), we constructed working curves for all trace elements, based on a range of MPI-DING (ATHO, STH5, T1, Jochum *et al.* 2000) and USGS glass standards (GSD, BCR), and ratioed against ^{30}Si (Supplementary Data file SD 2). It should be noted that all experimental glasses were microvesicular in nature owing to loss of volatiles upon quench. If the vesicles contained only exsolved volatiles and/or quench carbonate, their presence will lead to a reduction in the trace element and Si signal alike, and should thus not affect trace element quantification. Subsurface inclusions and contamination were monitored in a count-rate versus time plot and excluded from the averaging procedure. Molecular interferences were corrected for using conventional peak stripping, which meant that certain REE could not be constrained (e.g. low Eu concentrations are compromised by BaO interference). We additionally analysed experimental carbonates, using the same instrument conditions with a calcite standard from the Oka carbonatite complex (Quebec) for calibration, and ^{42}Ca as internal standard. Secondary standards were not available, but no major matrix effects are expected between a carbonatitic matrix and a carbonate mineral (see Blundy & Dalton, 2000). We observe a slight negative Gd anomaly in our dataset, which we suspect is due to problems in overcorrecting interferences.

Raman spectra were collected to distinguish between the expected polymorphs of $CaCO_3$ and SiO_2 in run products. We used a ThermoScientific DXR Raman Microscope at University of Bristol with a 532 nm laser at 5 cm^{-1} resolution over the spectral range 50–3500 cm^{-1}. The power was adjusted between 2 and 10 mW depending on sample fluorescence. Ten scans of 10 s each were collected and averaged, sometimes following 1 min of photobleaching.

RESULTS

General observations

Phase proportions in all experiments were obtained by unweighted least-squares regression, using anhydrous compositions and a reduced dataset. Phases that occur in trace amounts were excluded (Table 3, Fig. 2). Because of the presence of a hydrous silicic melt and a second, CO_2–H_2O-bearing fluid phase of unknown proportion and composition, mass balances could not be corrected for exsolved volatiles, as done by Klimm *et al.* (2008). (For the same reasons, mass balances cannot be made using hydrous compositions, because the amount of H_2O dissolved in the melt at run conditions cannot be constrained in the presence of a second fluid phase of unknown quantity and composition.) Mass-balance results are nevertheless in reasonable agreement with visual estimates obtained by SEM, especially for higher temperature runs containing few phases, or in the
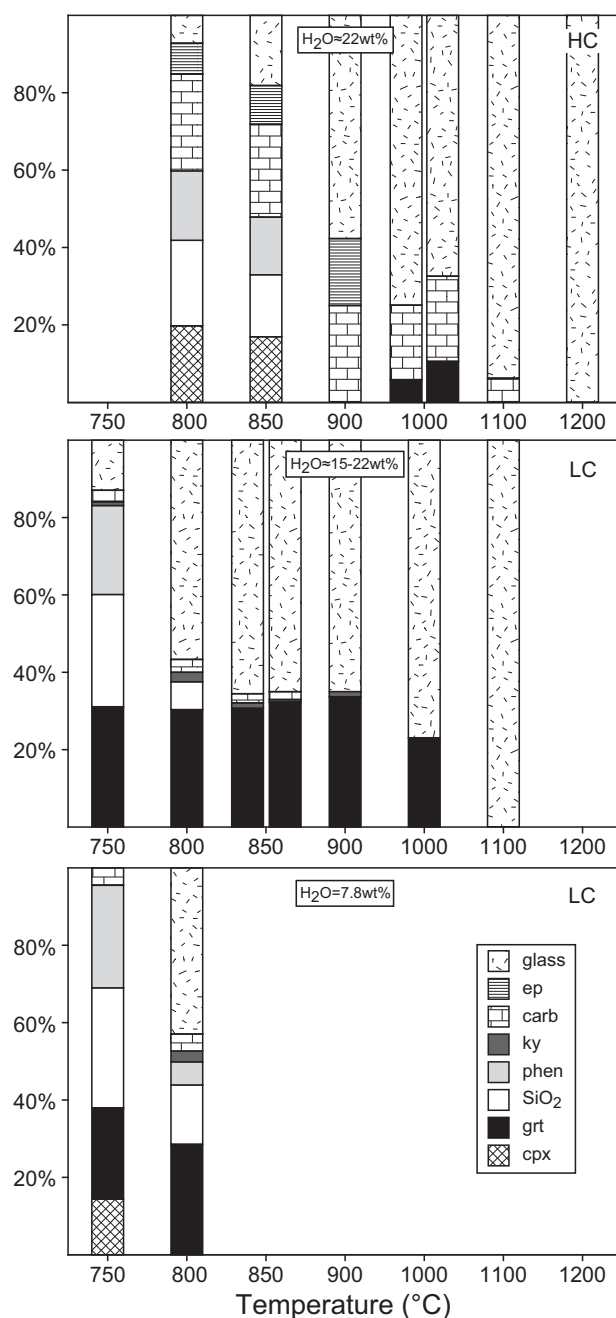

Fig. 2. Phase proportions in the experiments as a function of temperature and H_2O content. Data and mineral abbreviations are as in Table 3, in which trace and accessory phases are also indicated.

subsolidus runs. Problems in the mass-balance calculations for certain runs with large numbers of phases are probably due to degeneracy that results when one or more components can be expressed as linear functions of others (e.g. at a reaction). Mass balances for the problematic runs are replaced by visual estimates.

Representative SEM images of run products are given in Figs 3 (HC) and 4 (LC). Major element compositions of minerals are given in Supplementary Data file SD 3, and glasses in Tables 4 and 5. Figures 5 and 6 illustrate the systematic changes in the major element
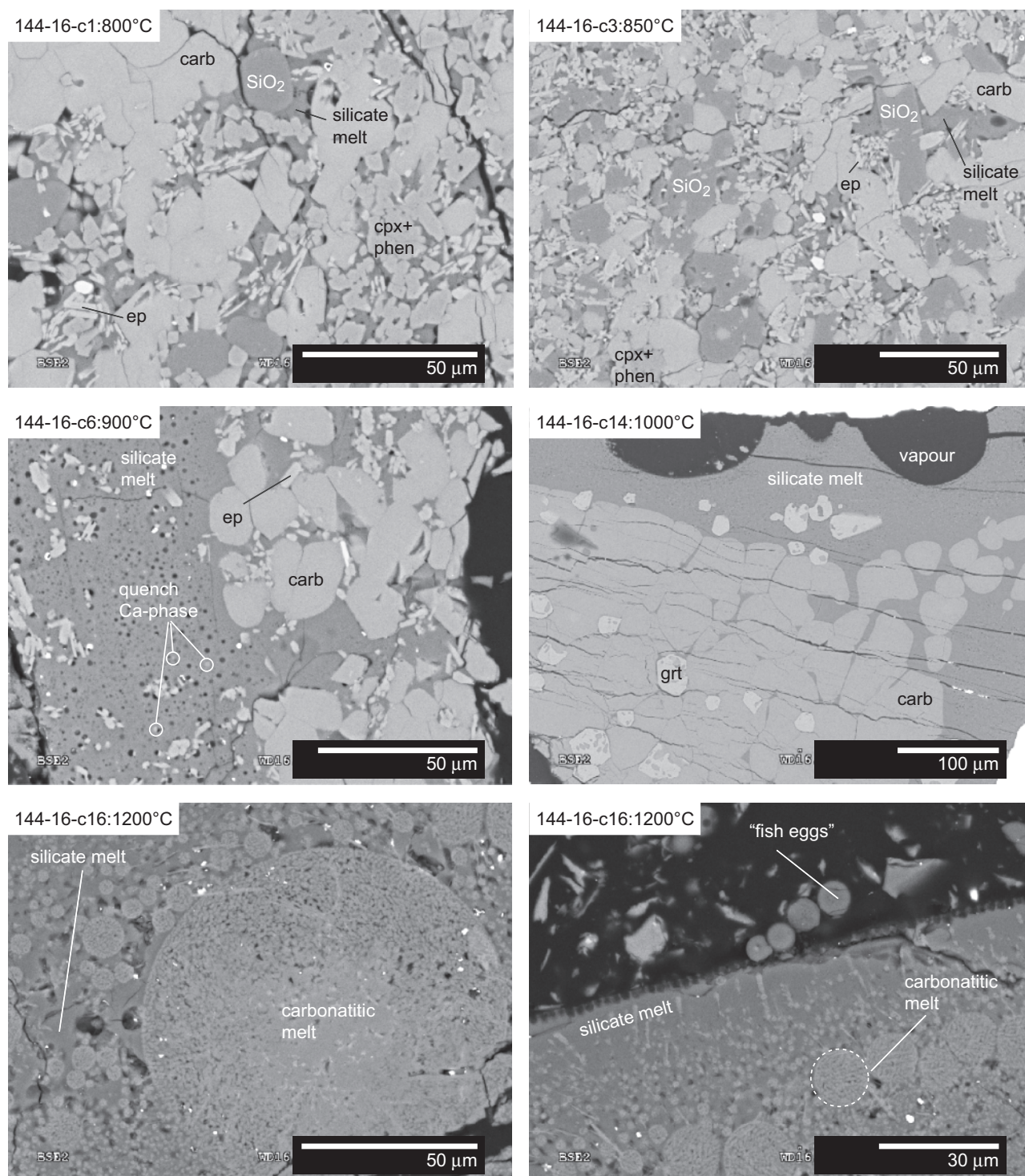
Fig. 3. Selected back-scattered electron (BSE) images of experimental run products at different temperatures in the HC experimental sequence (800–1200°C). Run numbers and mineral abbreviations are as in Table 3. Partial melts are always microvesicular, containing a Ca-rich quench phase. Clear evidence for an additional fluid phase, in the form of quenched solute spherules ('fish eggs'), is present in almost all experiments. Carbonates appear as prismatic crystals when surrounded by other silicates or carbonates; rounded crystals are more common when enclosed by melt only (see 1000°C experiment).

compositions of garnet, carbonate and glass as a function of temperature. We duplicated certain experiments to verify some of the results. All repeated supersolidus experiments agree well with each other, in terms of mass balance as well as mineral and glass chemistries (Figs 5 and 6; Tables 4 and 5). In addition, phase relations and chemistries generally agree with previous experiments on hydrated, calcareous sediments (Thomsen & Schmidt, 2008a; Tsuno & Dasgupta, 2012; Tsuno *et al.*, 2012, Mann & Schmidt (in press), as
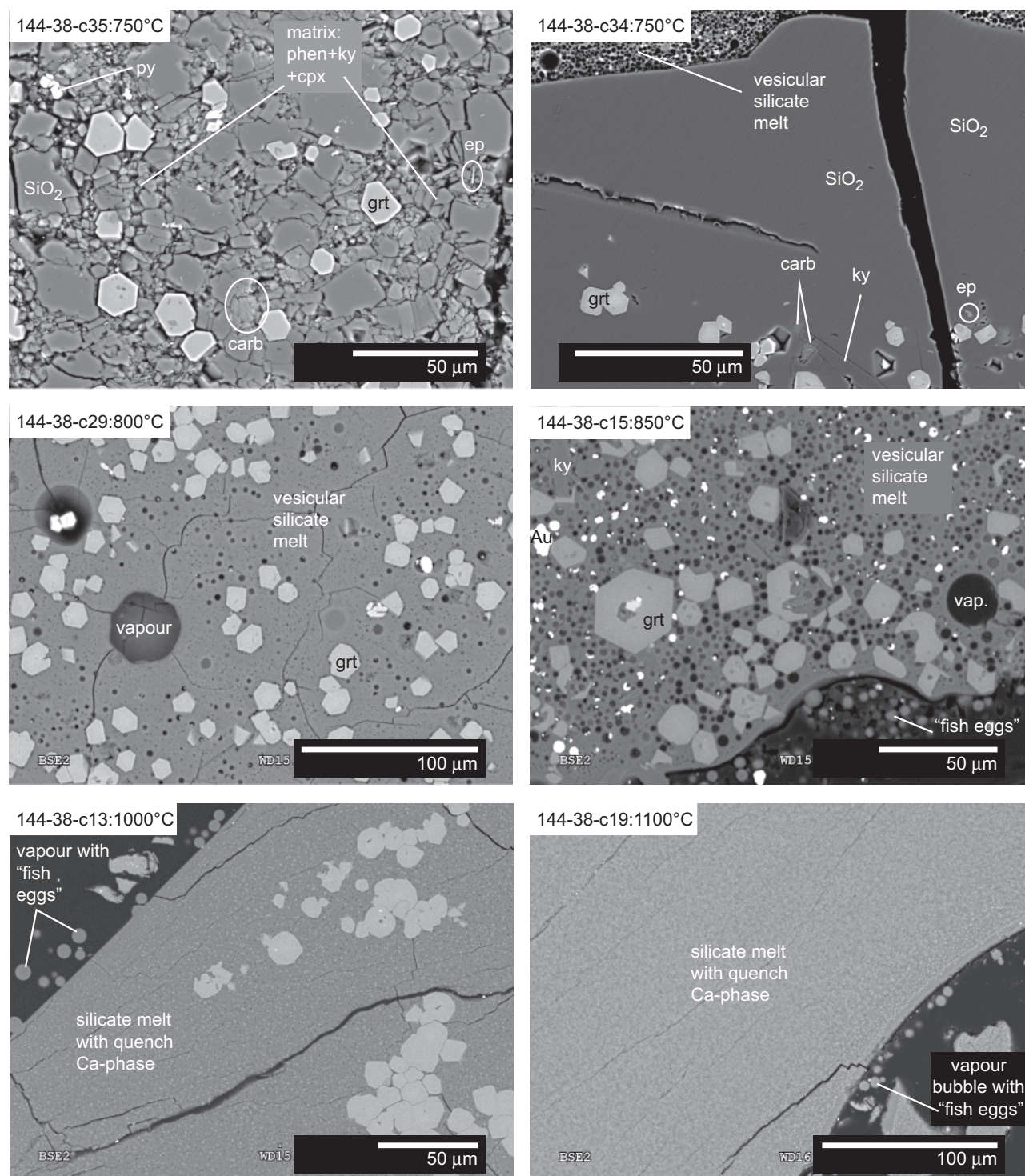
Fig. 4. Selected BSE images of experimental run products at different temperatures in the LC experimental sequence. Run numbers and mineral abbreviations are as in Table 3. As in Fig. 3, partial melts are always microvesicular and there is abundant evidence for an additional vapour phase. A carbonate-rich quench phase is always present in silicate glasses.

discussed below). The experiments performed at Bristol and at ETH are in good agreement in terms of phase petrology and the chemical compositions of glasses and silicates (Figs 5 and 6). Chemical homogeneity, reproducibility, and comparability within experimental limits with other studies suggest that the experiments

reached near-equilibrium conditions, with the exceptions of the static LC 800°C run products (Supplementary Data file SD 1).

All supersolidus experiments exhibit well-crystallized and relatively coarse-grained (*c.* 5–60 μm diameter) silicate and/or carbonate minerals, coexisting

Table 4: Major and minor element composition of experimental glasses in 144-16 (HC)

Exp.: 144-16-	c1	c1	c3	c3	c6	c6	c7	c7	c1	c3	c6	c7
Type:	meas	SD	meas	SD	meas	SD	meas	SD	anhydr	anhydr	anhydr	anhydr
T (°C):	800	800	850	850	900	900	1000	1000	800	850	900	1000
n:	10	10	9	9	14	14	20	20	10	9	14	20
SiO_2	64	2	65	1	64	2	51	2	76	77	76	63
TiO_2	0.12	0.02	0.17	0.02	0.25	0.02	0.49	0.03	0.14	0.20	0.30	0.61
Al_2O_3	13.2	0.6	12.3	0.2	11.5	0.4	13.0	0.4	15.6	14.5	13.7	16.2
FeO	0.8	0.3	0.9	0.2	1.3	0.2	2.2	0.3	1.0	1.0	1.6	2.7
MnO	0.01	0.01	0.01	0.02	0.02	0.03	0.05	0.04	0.01	0.01	0.02	0.06
MgO	0.13	0.09	0.12	0.04	0.19	0.05	0.8	0.2	0.15	0.14	0.23	1.0
CaO	1.7	0.6	1.6	0.6	2.2	0.5	9	2	2.1	1.8	2.6	11
Na_2O	2.3	0.5	1.6	0.3	1.2	0.2	1.6	0.2	2.8	1.9	1.4	1.9
K_2O	1.9	0.2	3.2	0.2	3.1	0.3	2.1	0.1	2.3	3.7	3.7	2.6
P_2O_5	0.08	0.02	0.13	0.03	0.14	0.06	0.13	0.04	0.09	0.15	0.17	0.16
Sum	85	2	85	1	84	2	80	2	100	100	100	100
Al/(K + Na + 2Ca)	1.5	0.2	1.4	0.2	1.2	0.1	0.61	0.07	1.5	1.4	1.2	0.61
(Na + K)/Al	0.45	0.06	0.49	0.05	0.46	0.05	0.37	0.03	0.45	0.49	0.46	0.37
Mg#	0.2	0.2	0.19	0.07	0.21	0.07	0.4	0.1	0.2	0.19	0.21	0.4

Exp.: 144-16-	c14	c14	c18	c18	c16	c16	c16*	c16*	c14	c18	c16
Type:	meas	SD	meas	SD	meas	SD	meas	SD	anhydr	anhydr	anhydr
T (°C):	1000	1000	1100	1100	1200	1200	1200	1200	1000	1100	1200
n:	22	22	46	46	33	33	5	5	22	46	33
SiO_2	57	1	40	2	38	2	6	2	69	54	50
TiO_2	0.50	0.03	0.43	0.05	0.37	0.05	0.3	0.2	0.61	0.57	0.49
Al_2O_3	13.0	0.4	10.3	0.6	9.6	0.4	1.5	0.5	15.7	13.7	12.6
FeO	1.94	0.09	3.1	0.5	2.8	0.7	3.4	0.5	2.34	4.1	3.7
MnO	0.04	0.03	0.06	0.04	0.07	0.04	0.10	0.05	0.05	0.09	0.09
MgO	0.64	0.04	1.4	0.2	1.3	0.3	1.8	0.3	0.78	1.8	1.7
CaO	6	1	17	1	21	1	45	1	8	22	27
Na_2O	1.13	0.08	0.8	0.1	1.1	0.2	0.20	0.03	1.36	1.1	1.4
K_2O	2.13	0.09	1.7	0.2	1.8	0.2	0.5	0.2	2.58	2.2	2.4
P_2O_5	0.14	0.04	0.13	0.04	0.12	0.03	0.15	0.03	0.17	0.17	0.15
Sum	83	1	75	2	76	1	59	2	100	100	100
Al/(K + Na + 2Ca)	0.84	0.07	0.31	0.02	0.23	0.01	0.02	0.01	0.84	0.31	0.23
(Na + K)/Al	0.32	0.02	0.31	0.03	0.39	0.05	0.6	0.3	0.32	0.31	0.39
Mg#	0.37	0.03	0.44	0.09	0.4	0.1	0.5	0.1	0.37	0.44	0.4

*carbonatitic liquid.

with abundant microvesicular glass (= quenched melt). Most runs show clear evidence for a coexisting fluid phase that often contains 'fish egg' textured spherules <2–5 μm in diameter (Figs 3 and 4) that are thought to represent the quenched silicate fraction of a solute-rich fluid phase (see Adam et al., 1997). Residual silicate phases disappear progressively up to temperatures of 1000°C (Fig. 2). An immiscible carbonatite liquid appears at temperatures of 1000–1100°C in HC, and crystalline carbonate persists to between 1100 and 1200°C. Carbonate in LC disappears from the solid assemblage at 900°C.

Subsolidus and near-solidus experiments tend to contain crystal-rich 'islands', separated by large vesicles that are now filled by epoxy. Within these vesicles 'fish egg' textured spherules, as well as other silicates and carbonates, are often preserved, suggesting that they represent space that was formerly occupied by a fluid. Another characteristic of the subsolidus experiments is the generally smaller grain sizes of all phases apart from SiO_2, as well as less well-developed crystal faces.

Mineral chemistry

Ferric iron contents were computed by the method of Droop (1987) for garnet and clinopyroxene. For other minerals, such as epidote, stoichiometric considerations were used for estimation of Fe^{3+}. Garnets occur in LC experiments from subsolidus (750°C) to liquidus (≤1100°C) conditions. They appear as (sub-)idiomorphic, coarse-grained (10–40 μm diameter) crystals, which may contain inclusions. LC garnets are rich in almandine (47–56%), grossular (19–30%) and pyrope (14–29%), but poor in spessartine (≤1%) and andradite (0–3%) (Fig. 5). With increasing temperature pyrope contents increase, mostly at the expense of almandine, such that Mg# [defined as molar $Mg/(Mg + Fe^{2+})$] increases from 0.19 to 0.37. This pattern is consistent with experimental, eclogitic garnets in both calcareous (e.g. Thomsen & Schmidt, 2008a; Tsuno & Dasgupta, 2012) and carbon-free sediments (e.g. Hermann & Spandler, 2008; Skora & Blundy, 2010), as well as exhumed high-pressure metamorphic terrains that contain pyrope-rich garnets (e.g. Chopin, 1984; Terry et al., 2000; Wei et al., 2009). In HC experiments garnets appear only at 1000°C. They are significantly richer in grossular (43–47%) and andradite (3–5%) than in LC charges owing to the high bulk CaO and Fe_2O_3 of the HC compositions, and poorer in almandine (31–35%) and pyrope (16–17%) (Fig. 5). Despite the differences, these garnets have Mg# of 0.33 at 1000°C, comparable with those in LC experiments (Fig. 5).

Table 5: Major and minor element composition of experimental glasses in 144-38 (LC)

Exp.: 144-38-	c34	c34	c28	c28	c29	c29	c4	c4	c34	c28	c29	c4
Type:	meas	SD	meas	SD	meas	SD	meas	SD	anhydr	anhydr	anhydr	anhydr
T (°C):	750	750	800	800	800	800	850	850	750	800	800	850
n:	10	10	23	23	22	22	39	39	10	23	22	39
SiO_2	58	2	67	1	67	1	60	4	75	74	74	75
TiO_2	0.14	0.04	0.19	0.02	0.19	0.03	0.18	0.02	0.18	0.21	0.21	0.23
Al_2O_3	10.5	0.4	13.2	0.3	12.8	0.1	10.5	0.7	13.6	14.7	14.2	13.2
FeO	0.4	0.3	0.9	0.2	0.8	0.1	1.2	0.2	0.6	1.0	0.9	1.5
MnO	0.01	0.02	0.02	0.03	0.02	0.02	0.02	0.02	0.02	0.02	0.02	0.03
MgO	0.20	0.04	0.33	0.07	0.49	0.05	0.53	0.06	0.25	0.36	0.54	0.67
CaO	1.5	0.3	1.8	0.3	2.6	0.4	2.0	0.3	1.9	2.1	2.8	2.5
Na_2O	3.2	0.7	2.8	0.3	2.0	0.2	1.4	0.3	4.1	3.1	2.2	1.7
K_2O	3.3	0.2	4.1	0.2	4.2	0.1	3.5	0.2	4.2	4.6	4.6	4.4
P_2O_5	0.15	0.04	0.11	0.03	0.13	0.03	0.20	0.07	0.19	0.12	0.14	0.25
Sum	78	3	90	1	91	1	79	4	100	100	100	100
Al/(K+Na+2Ca)	0.9	0.1	1.07	0.06	1.02	0.05	1.1	0.1	0.9	1.07	1.02	1.1
(Na+K)/Al	0.8	0.1	0.68	0.04	0.62	0.02	0.58	0.06	0.8	0.68	0.62	0.58
Mg#	0.4	0.3	0.4	0.1	0.52	0.09	0.45	0.08	0.4	0.4	0.52	0.45

Exp.: 144-38-	c15	c15	c11	c11	c13	c13	c19	c19	c15	c11	c13	c19
Type:	meas	SD	meas	SD	meas	SD	meas	SD	anhydr	anhydr	anhydr	anhydr
T (°C):	850	850	900	900	1000	1000	1100	1100	850	900	1000	1100
n:	15	15	20	20	24	24	29	29	15	20	24	29
SiO_2	63	3	63.4	0.5	56.3	0.8	50	1	76	73.7	67.9	62
TiO_2	0.19	0.02	0.29	0.02	0.71	0.03	0.71	0.03	0.23	0.33	0.85	0.87
Al_2O_3	11.1	0.5	11.5	0.1	12.8	0.2	12.8	0.3	13.4	13.4	15.5	15.6
FeO	1.2	0.1	1.7	0.1	2.5	0.2	3.7	0.3	1.4	2.0	3.1	4.6
MnO	0.02	0.02	0.04	0.03	0.04	0.03	0.09	0.04	0.02	0.05	0.05	0.10
MgO	0.42	0.02	0.66	0.05	1.09	0.07	2.0	0.2	0.51	0.76	1.32	2.4
CaO	1.9	0.2	3.0	0.3	5.8	0.5	8.8	0.9	2.3	3.5	6.9	10.7
Na_2O	1.5	0.2	1.3	0.1	1.13	0.08	1.1	0.1	1.8	1.5	1.36	1.3
K_2O	3.6	0.2	3.9	0.1	2.38	0.08	2.2	0.1	4.3	4.6	2.86	2.6
P_2O_5	0.21	0.02	0.17	0.03	0.17	0.04	0.13	0.03	0.26	0.19	0.20	0.16
Sum	83	4	86.0	0.5	83.0	0.9	82	1	100	100	100	100
Al/(K+Na+2Ca)	1.13	0.08	0.96	0.04	0.86	0.04	0.63	0.04	1.13	0.96	0.86	0.63
(Na+K)/Al	0.58	0.05	0.56	0.02	0.34	0.01	0.32	0.02	0.58	0.56	0.34	0.32
Mg#	0.39	0.04	0.41	0.05	0.43	0.04	0.48	0.06	0.39	0.41	0.43	0.48

Omphacitic clinopyroxenes occur in 800–850°C HC runs. They tend to form small (~5–10 μm diameter), tabular to prismatic crystals with a significant jadeite component (~60–70%), and a smaller quadrilateral (QUAD) Ca–Mg–Fe component (~30–40%). The LC clinopyroxene at 750°C has a different composition, being richer in QUAD (56%) and poorer in jadeite (34%).

Carbonates in the HC experiments were calcium carbonate solid solutions (ss) with 0.6–3.2 wt % MgO and 0.5–3.9 wt % FeO. Molar Ca fractions [X_{Ca} = Ca/(Ca + Mg + Fe)] vary systematically with temperature from 0.91–0.88 at 800–900°C to 0.93–0.98 at 1000–1100°C. Texturally, carbonates appear as prismatic or rounded crystals 10–40 μm in size (40–80 μm at 1000°C). Rounded crystals are more common when enclosed by melt, whereas prisms are more common when surrounded by other silicates or carbonates. It was initially expected that aragonite would be stable at our chosen P–T conditions, based on data for both the pure $CaCO_3$ system and the addition of minor $MgCO_3$ (Hacker et al., 2005). However, Raman spectra of our run products over the whole carbonate stability range indicate that only calcite is present. It appears that the high Mg and Fe content lowered the 3 GPa calcite–aragonite transition temperature. Carbonates in the LC experiments also form sub-

idiomorphic to prismatic crystals, but they tend to be finer grained than their HC counterparts and are much richer in MgO (9.8–15.8 wt %) and FeO (4.9–13.5 wt %), exhibiting Fe-rich, near-dolomitic compositions. Despite major differences in X_{Ca} (0.55–0.60), Mg# values are similar in both experimental sequences (0.57–0.85) and are comparable with those of Thomsen & Schmidt (2008a).

Epidote–clinozoisite$_{ss}$ ('epidote' hereafter) occurs in 750–850°C LC experiments, as well as in 800–900°C HC experiments. In both bulk compositions epidotes exhibit almost equal proportions of the end-members epidote [$Ca_2Al_2(Fe^{3+};Al)(Si_3O_{12})(OH)$] and clinozoisite [$Ca_2Al_2(Al)(Si_3O_{12})(OH)$]: for HC, $X_{ep} \approx 0.4–0.5$, and for LC, $X_{ep} \approx 0.4–0.7$. Epidotes were not reported by Thomsen & Schmidt (2008a), Tsuno & Dasgupta (2012), Tsuno et al. (2012) or Mann & Schmidt (in press), but zoisite is present in the KCMASH experiments of Thomsen & Schmidt (2008b). The presence or absence of either of these phases is a complex function of P, T and bulk-rock chemistry (e.g. Fe^{3+}, Fe^{tot}, Ca and fO_2; e.g. Holdaway, 1972; Liou, 1973; Liou et al., 1983).

An SiO_2 phase is present in appreciable quantities at low temperatures in both lithologies. For two of the 800°C runs (144-16-c1 and 144-38-c12) the Raman spectra show this phase to be quartz, but for
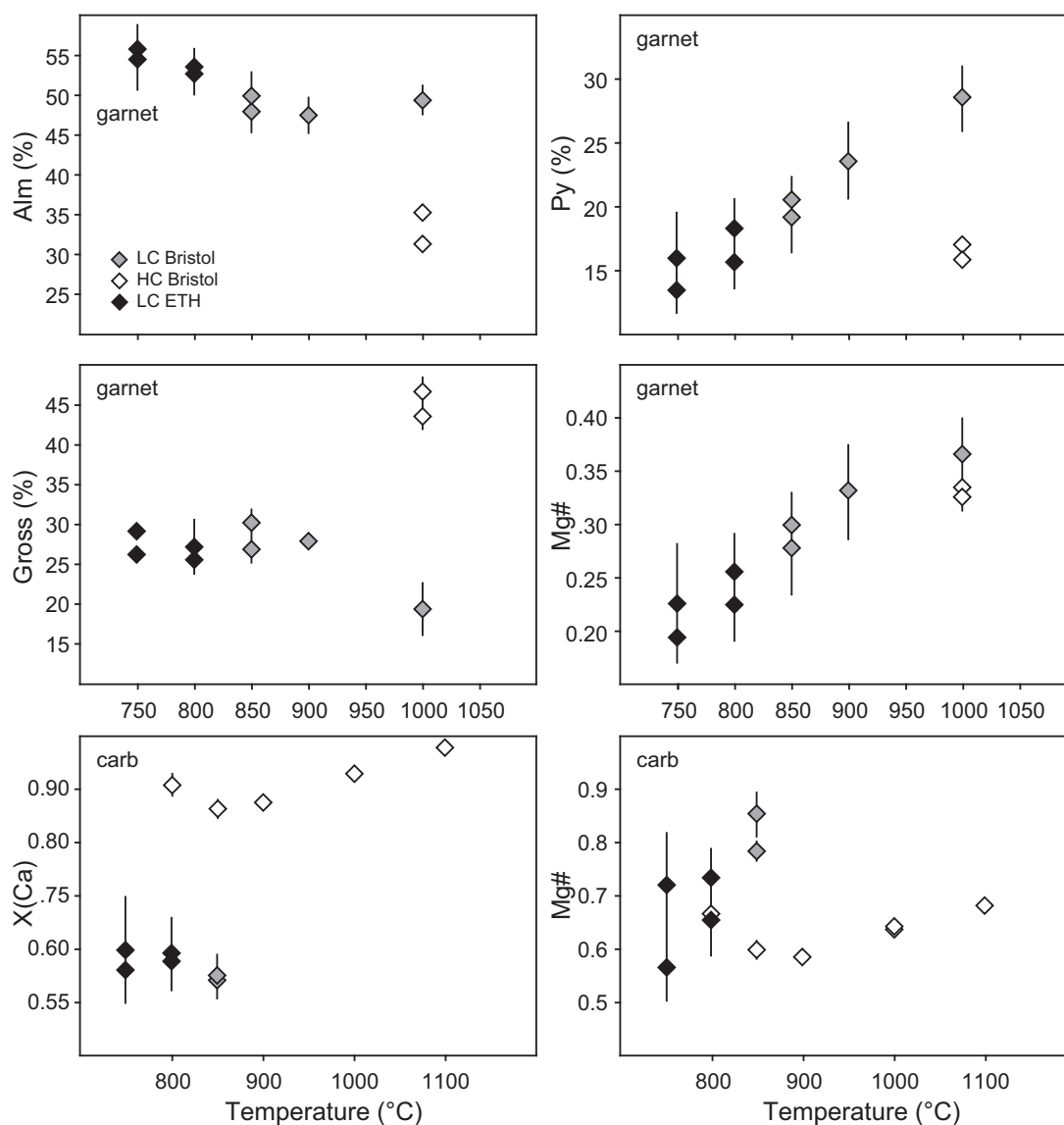
Fig. 5. Major element chemistry of garnet and carbonate shows systematic changes with temperature. Carbonate compositions appear to be bulk-rock dependent, and change with increasing temperature towards slightly more calcite-rich compositions. LC experiments labelled 'ETH' are those performed using the rocking apparatus. The very good agreement between the Bristol and ETH runs should be noted.

the other static 800°C run (144-38-c20) and all runs at 850°C, it is coesite. Coesite is the expected phase at a nominal pressure of 3 GPa for both temperatures, suggesting that the two 800°C runs with quartz were perhaps conducted at only 2·95 GPa (Bose & Ganguly, 1995), which is within the expected pressure uncertainty of the Bristol piston cylinder (McDade *et al.*, 2002).

Rectangular phengite (~5–10 μm diameter; Si atoms per formula unit = 3·3–3·5) is the main host for K_2O at temperatures up to 850°C. Other minor phases include Fe-bearing ($Fe_2O_3 \approx$ 0·5–1 wt %) kyanite (LC only) at 800–900°C, rutile at $T \leq 1000$°C (in both lithologies), and hematite–ilmenite (800–900°C, LC only). Hematite–ilmenite is absent in the repeated LC experiments that appear to have experienced slightly lower fO_2 conditions (see below).

Melting temperatures, reactions and textures of quenched glasses

The solidus temperature was bracketed for LC only. At 750°C and 7·8 wt % H_2O, glass pools that could represent a melt phase are absent. Texturally, this run is characterized by large voids, with some 'fish eggs', suggesting the presence of a solute-rich fluid. Crystal-rich parts of the run product contain abundant phengite, carbonate, SiO_2, and clinopyroxene as well as other trace and accessory phases (Table 3). The coexistence of abundant phengite with substantial excess water (~7%) is additional evidence that this run did indeed experience subsolidus conditions [see, e.g. figure 18 of Skora & Blundy (2010)], even in the hot centre, which was at around 760°C. The fact that melt is clearly present at 800°C suggests that 760°C < $T_{solidus}$ < 800°C. The 750°C
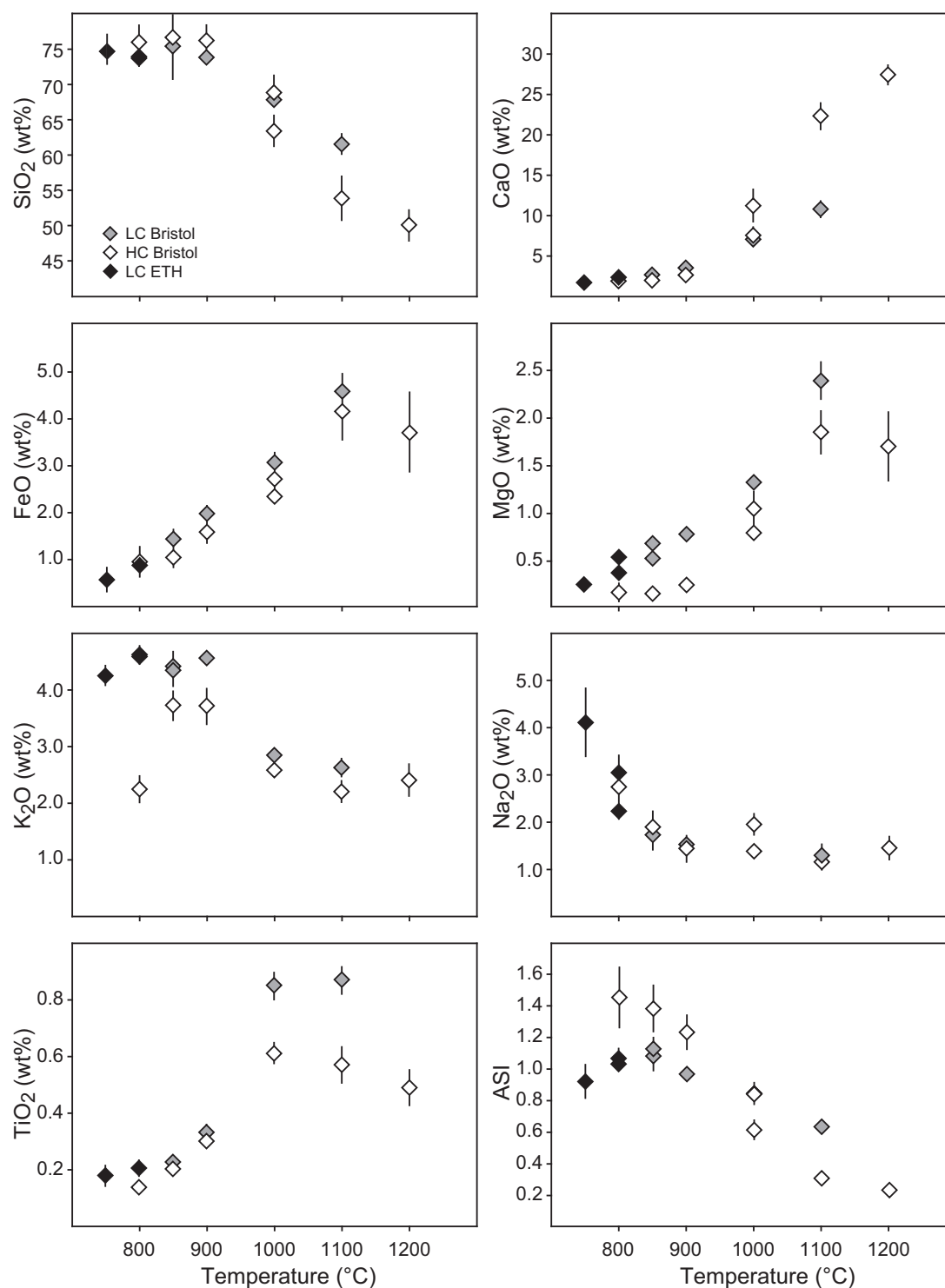
Fig. 6. Major element chemistry of quenched glasses shows systematic changes with temperature in accordance with changing phase petrology (see text for detail). Molar Al/(Na + K + 2Ca) (ASI) ratios of quenched glasses exhibit trends from peraluminous to metaluminous compositions at higher temperatures. The very good agreement of LC experiments performed in different laboratories should be noted.

run that contained 15 wt % H_2O exhibits a comparable phase assemblage, albeit with more voids and 'fish eggs', and no clinopyroxene. Interestingly, this run exhibits some vesicular melt pools (Fig. 4) alongside abundant 'fish eggs'. The melt pools can be found only

in the central part of the run product, which represents the hottest part of the capsule with a modelled peak temperature of around 760°C. This observation further refines the solidus temperature given that this is the only point where phengite, fluid and melt can coexist.

The elevated garnet fraction, as well as the absence of clinopyroxene, is taken as additional evidence that melting had commenced in this run, given that clinoyproxene is typically consumed and garnet produced during melting (e.g. Thomsen & Schmidt, 2008a; discussed further below). The apparent difference in melting temperature between these two runs is unlikely to be related only to temperature as the modelled peak temperatures are almost identical (758 and 761°C). The reason for this difference is discussed below.

At 800°C melt (glass) is produced at the expense of phengite, SiO_2 and clinopyroxene and minor carbonate (LC only). The melting reaction appears to produce garnet (LC only), which at $T > 900$°C dissolves congruently into the melt until the liquidus is crossed at 1000–1100°C. Epidote is produced alongside melt in HC in place of garnet. At higher temperatures (900–1000°C) garnet appears in HC runs and melt fraction increases at the expense of epidote and carbonate. Garnet appears at similar temperatures in the KCMASH experiments of Thomsen & Schmidt (2008b). Garnet and carbonate then dissolve congruently into the melt at temperatures over 1000°C until the liquidus is crossed between 1000 and 1100°C. A carbonatitic melt appears at 1100°C in HC runs, consistent with carbonatite-in as determined by Thomsen & Schmidt (2008a). This is suggested by the coexistence of carbonate, fluid, carbonatite melt and silicate melt at 1100°C and fluid, carbonatite melt and silicate melt at 1200°C (Fig. 3).

All supersolidus experiments contain quenched silicate glasses that exhibit (1) microvesicles, (2) large vesicles or voids that may or may not contain additional 'fish eggs', and (3) microvesicles that are filled with a Ca-rich phase (Figs 3 and 4). Similar textures were described by Thomsen & Schmidt (2008a; see their figure 2l). Microvesicles (1) are common in quenched glasses in water-rich experiments and are ascribed to the fact that the maximum amount of water that can be quenched into glasses produced in piston cylinder apparatus (~8–10 wt %, Kadik & Lebedev, 1968; McMillan & Holloway, 1987; Paillat *et al.*, 1992) is much less than the equilibrium amount dissolved at high *P–T* run conditions (20–35 wt %, Kessel *et al.*, 2005).

The walls of the set of larger vesicles (2) are often decorated with 'fish eggs', suggesting that these represent a fluid phase formerly rich in dissolved silicates ('siliceous fluid'), which coexisted with melt at run conditions. Hence, the melt is demonstrably subcritical at 3 GPa and 800–1200°C (see, e.g. Manning, 2004), in broad agreement with experimental studies on other hydrated, calcareous sediments (Thomsen & Schmidt, 2008a, 2008b; Tsuno & Dasgupta, 2012; Mann & Schmidt (in press)), which all show evidence of a second fluid phase coexisting with silicate glass. However, this contrasts with observations on melting of carbon-free sediments that apparently lack evidence for a coexisting fluid phase at similar conditions (Hermann & Spandler, 2008), suggesting that these partial melts represented supercritical fluids (e.g. Hermann *et al.*,

2006). Given that both CO_2-free and CO_2-bearing pelites produce broadly similar (granitic) melts at near-solidus temperatures, it would appear that the presence of CO_2 affects the stability field of fluid + melt and, in consequence, the location of the second critical endpoint in the system granite–H_2O–CO_2.

Microvesicles filled with a Ca-rich phase (3) are difficult to interpret. They are too small to be measured by EMPA, but visual inspection of SEM spectra suggests that these have a large carbonate component. The fact that they fill microvesicles suggests that this is a quench product. Hence, we interpret the Ca-rich phase to represent some of the carbonate component once dissolved in the silicate melt. True carbonatite immiscible liquids are present in HC at temperatures over 1100°C. They form subspherical features in the silicate glasses (Fig. 3), exhibiting internal dendritic or amoeboidal quench textures [see also Thomsen & Schmidt (2008a) and review by Brooker & Kjarsgaard (2011)].

Glass compositions

Experimental silicate glasses are relatively homogeneous in major elements (1σ of around ± 3–10% relative, minor elements up to ± 20% relative; Table 4 (HC); Table 5 (LC)] apart from CaO (around ± 20%), which is attributed to an irregular distribution of voids that are filled with the quench carbon phase (Figs 3 and 4). The only exception is the 750°C experiments where variations are larger. This is probably related to the fact that full equilibration is hampered when melt pools are not interconnected through a coexisting fluid phase, but rather occur as 'islands'. Near-solidus silicate melts are rich in SiO_2, Al_2O_3, CaO, K_2O and Na_2O, and can be classified as peraluminous to metaluminous granitic melts. The ASI index [molar Al/(Na + K + 2Ca)] is 0·9–1·1 at 750–900°C in LC experiments and 1·2–1·5 in HC experiments. Glass compositions from experiments at 1000°C are metaluminous, subalkaline granodioritic in composition [LC ASI ~ 0·9 and molar (Na + K)/Al ~ 0·3; HC ASI ~ 0·6–0·8 and (Na + K)/Al ~ 0·3–0·4]. ASI values increase from 750 to 800°C then decrease systematically with increasing temperatures (Fig. 6). Eventually, the increasing CaO content, concomitant with the decrease of $CaCO_3$ as a residual phase, forces the melt into a silicate–carbonate two-liquid immiscible field (see Brooker & Kjarsgaard, 2011). These compositions and chemical trends are consistent with other published studies on partial melting in calcareous systems and show some similarity to carbon-free sediments at similar *P–T* conditions (e.g. Nichols *et al.*, 1994; Johnson & Plank, 1999; Schmidt *et al.*, 2004; Hermann & Spandler, 2008; Thomsen & Schmidt, 2008a; Skora & Blundy, 2010; Tsuno & Dasgupta, 2012).

Single melt components show good correlation with phase stabilities as a function of increasing temperature (Fig. 6). The peak in SiO_2 around 850°C and its subsequent decline reflects exhaustion of SiO_2 during melting. CaO, FeO and MgO increase steadily, reflecting

progressive dissolution of carbonate, epidote and garnet. The Mg# of melts coexisting with garnet (LC: 750–1000°C; HC: 1000°C) is around 0·37–0·52, whereas the Mg# of garnets is lower (0·23–0·37). Garnet–melt Fe–Mg partition coefficients are consistent with the study of Ellis (1986) in that $Mg\#_{melt} > Mg\#_{grt}$ at 750–900°C and $Mg\#_{melt} \approx Mg\#_{grt}$ at 1000°C at 3 GPa. Melts in equilibrium with epidote ± clinopyroxene (HC: 800–900°C) have Mg# of around 0·2. Potassium contents are high in the presence of phengite; upon its exhaustion at around 850°C K_2O decreases through dilution. Sodium systematically decreases as a result of dilution, consistent with the absence of clinopyroxene in the presence of melt. All these geochemical characteristics are consistent with those reported in previous studies, summarized in figure 5 of Tsuno & Dasgupta (2012). The only real difference in our study is that certain changes in melt chemistry (e.g. increase in CaO, MgO and FeO; decrease in SiO_2), occur at lower temperatures reflecting earlier exhaustion of certain minerals as a response to increased melting owing to elevated initial H_2O.

Carbonatitic liquids exhibit typical immiscible textures (e.g. Kjarsgaard, 1998; Martin *et al.*, 2013). Measurements with a defocused beam suggest that these liquids have significant SiO_2 (6·3 ± 1·7 wt %), FeO (3·4 ± 0·6 wt %), MgO (1·8 ± 0·3 wt %) and Al_2O_3 (1·5 ± 0·5 wt %), with alkalis only in minor quantities (Na_2O: 0·20 ± 0·03 wt %; K_2O: 0·49 ± 0·25 wt %). We would view the alkali contents of the carbonatitic liquid as uncertain, because the sample preparation technique, involving water, was not optimized to prevent alkali loss (e.g. Martin *et al.*, 2013).

Trace element concentrations

Trace elements concentrations in the experimental glasses are given in Table 6 and are plotted in Fig. 7a and b. Trace elements can be roughly classified as incompatible, partitioning-controlled, or solubility-controlled. Incompatible elements follow a simple dilution trend as melt fraction increases with temperature. A partitioning-controlled element is redistributed between solid and melt as a function of the weighted sum of mineral–melt partition coefficients (*D* values). In practice, bulk *D* values for single trace elements are often dominated by the *D* values of just one or two minerals [e.g. Y + heavy REE (HREE) in garnet; Nb + Ta in rutile; Hf in zircon; Ba in phengite; Sr in carbonate]. For a given trace element the concentration in the melt is a function of the initial concentration, the melt fraction and the proportion of the key residual mineral(s). Solubility-controlled elements are those that constitute an essential (or dominant) structural component in a particular, usually accessory phase. A straightforward example is TiO_2, whose concentration in the melt is entirely controlled by rutile solubility. Zirconium is controlled by zircon solubility, at least in SiO_2-saturated systems. Light REE (LREE) can be regarded as controlled by monazite/allanite solubility, although their solubility behaviour can become more

complicated (e.g. Skora & Blundy, 2012). The main difference from partitioning-controlled elements is that the absolute concentration of a solubility-controlled element is limited only by its solubility in the host mineral at the *P–T* of interest, regardless of the initial concentration. An important feature of both partitioning-controlled and solubility-controlled elements is that their concentrations in melts reach a maximum at the point when the relevant host phase is exhausted from the residue (e.g. Klemme *et al.*, 2002).

Caesium behaves almost perfectly incompatibly in the experimental partial melts, reflecting the lack of a
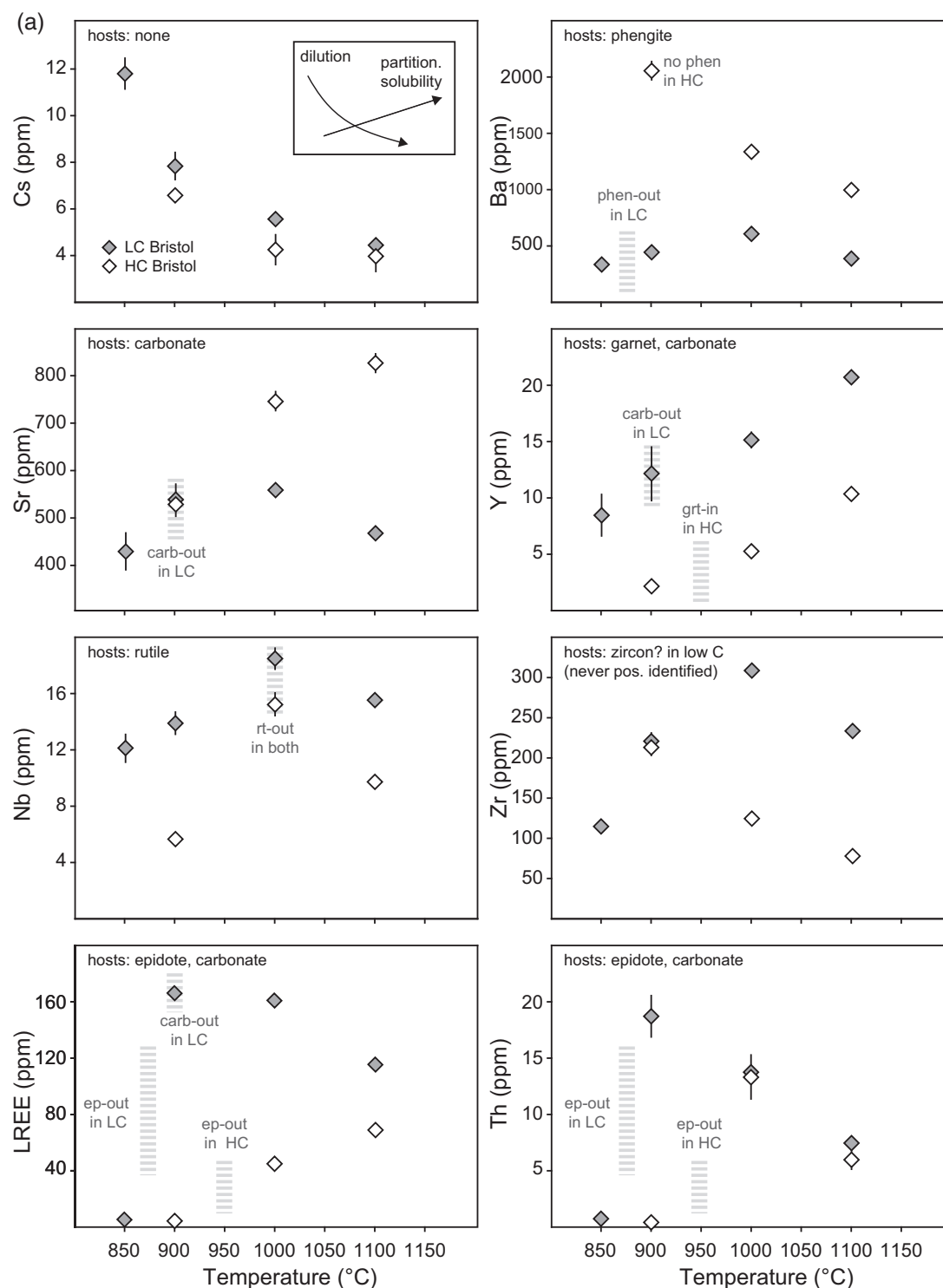
Table 6: Trace element composition of silicate glasses

144-38- Type: T (°C): n:	bulk*	c15 meas 850 5	c15 SD 850 5	c11 meas 900 5	c11 SD 900 5	c13 meas 1000 5	c13 SD 1000 5	c19 meas 1100 4	c19 SD 1100 4
Rb	93·3	219	7	217	9	135	4	108	8
Sr	349	425	41	536	34	556	5	464	10
Y	25·4	9	2	12	2	15·2	0·7	20·7	0·2
Zr	167	115	9	221	11	308	2	233	2
Nb	12·8	12	1	13·9	0·8	18·4	0·8	15·5	0·5
Cs	4·64	11·7	0·7	7·8	0·6	5·5	0·2	4·4	0·2
Ba	228	337	21	446	27	610	8	390	14
La	29·4	1·3	0·3	40	1	40·6	0·7	27·0	0·4
Ce	61·9	2·1	0·3	83	4	76	2	54·1	0·9
Pr	7·12	0·2	0·1	8·3	0·4	7·5	0·2	5·6	0·2
Nd	26·9	1·3	0·5	31	1	32	2	24·4	0·4
Sm	5·5	0·8	0·4	4·4	0·7	5·3	0·4	4·4	0·3
Gd	4·83	1·4	0·9	2·8	0·6	4	1	3·8	0·6
Dy	4·57	1·4	0·4	2·3	0·5	2·9	0·2	4·0	0·5
Ho	0·912	0·3	0·1	0·4	0·1	0·57	0·04	0·74	0·03
Lu	0·37	0·14	0·03	0·19	0·05	0·17	0·02	0·31	0·02
Hf	4·21	4·0	0·5	6·8	0·5	8·2	0·5	5·6	0·7
Ta	0·886	0·9	0·1	0·9	0·1	1·35	0·08	0·90	0·09
Th	8·19	0·8	0·2	19	2	13·7	0·6	7·5	0·3
U	1·61	2·0	0·3	3·6	0·3	2·9	0·2	1·3	0·1
ΣLREE	131	5·7	0·8	166	5	161	3	115	1
Ba/Th	28	416	85	24	3	44	2	52	3
(La/Sm)$_{PUM}$	3·6	1·2	0·6	6	1	5·1	0·4	4·1	0·3
(U/Th)$_{bulk}$	1	13	3	1·0	0·1	1·1	0·1	0·9	0·1

144-16- Type: T (°C): n:	bulk*	c6 meas 900 5	c6 SD 900 5	c14 meas 1000 5	c14 SD 1000 5	c18 meas 1100 4	c18 SD 1100 4
Rb	56·2	146	4	96	6	90	3
Sr	986	524	26	746	22	826	22
Y	16·8	2·2	0·2	5·4	0·6	10·4	0·5
Zr	68·6	213	10	125	6	79	2
Nb	8·27	5·7	0·3	15·2	0·8	9·7	0·4
Cs	3·52	6·6	0·3	4·2	0·5	4·0	0·7
Ba	943	2054	87	1337	29	999	23
La	20·6	1·9	0·2	13·0	0·6	18·4	0·6
Ce	38·3	1·2	0·5	21	2	31	1
Pr	4·83	0·10	0·05	2·0	0·3	3·5	0·2
Nd	17·8	0·6	0·5	8·1	0·7	14·0	0·8
Sm	3·34	0·2	0·1	1·2	0·2	2·5	0·4
Gd	2·76	1·9	0·3	1·3	0·3	2·3	0·6
Dy	2·5	0·6	0·2	0·9	0·3	1·8	0·5
Ho	0·52	0·26	0·02	0·29	0·04	0·39	0·05
Lu	0·22	0·06	0·01	0·09	0·06	0·15	0·03
Hf	1·68	6·0	0·6	3·8	0·3	2·1	0·1
Ta	0·55	0·8	0·1	1·2	0·2	0·72	0·07
Th	7·11	0·38	0·06	13	2	6·0	0·9
U	0·97	0·92	0·09	2·2	0·4	0·7	0·2
ΣLREE	84·9	4·0	0·7	45	2	69	1
Ba/Th	133	5420	940	100	15	166	26
(La/Sm)$_{PUM}$	4·1	6	4	7	1	4·9	0·8
(U/Th)$_{bulk}$	1	18	3	1·2	0·3	0·9	0·2

*From Carpentier *et al.* (2008).

Fig. 7. (a) Trace element contents of quenched experimental glasses as a function of temperature. Selected trace elements are representative of classes of behaviour; for example, Cs representing incompatible elements; Ba being controlled by the presence or absence of phengite; Sr by carbonate; Y by garnet and carbonate; Nb by rutile, Zr probably by zircon (LC only); LREE + Th by epidote and carbonate. Key phase boundaries are shown by broad grey banded lines. (Error bars are 1σ.)(b) Trace element ratios of quenched experimental glasses as a function of temperature. These ratios were selected because they are often used to characterize the slab component in arc lavas (e.g. Elliott, 2003). Key phase boundaries are shown by broad grey banded lines. (Error bars are 1σ.)
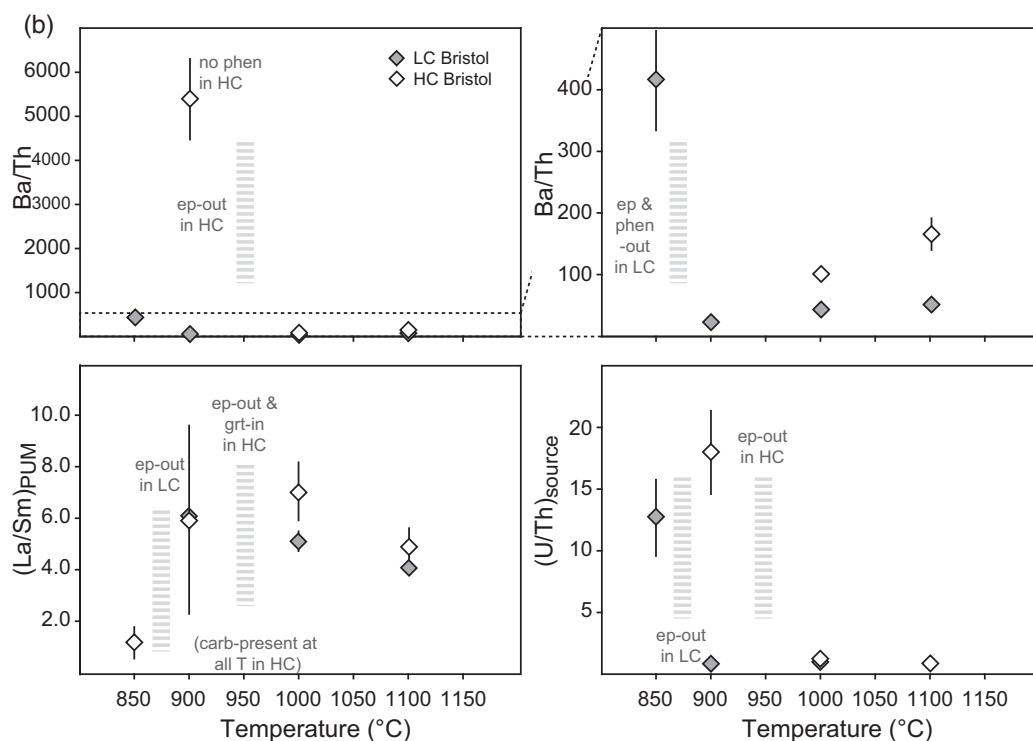
Fig. 7. Continued

suitable residual host phase. Barium and Rb are also incompatible in the HC experiments at $T \geq 900°C$ owing to the absence of phengite. Strontium, partly hosted by carbonate (Supplementary Data file SD 4), and potentially by epidote at lower temperatures, steadily increases with temperature in both lithologies. In LC Sr then follows a dilution path at $T > 900°C$ when carbonate and epidote become exhausted. This is a very similar pattern to Ba and Rb (LC) and Nb and Ta (both lithologies), where concentrations slightly increase until their respective hosts phengite (LC) and rutile (both lithologies) are exhausted at around 850–900 and 1000°C, respectively. Zirconium is expected to be controlled by zircon solubility in partial melts of subducted sediments (e.g. Rubatto & Hermann, 2007). Although no zircon was found in our run products the pattern of an increase followed by a decrease at $T > 1000°C$ in LC is consistent with the presence of trace amounts of zircon that are melting out. The Zr pattern of HC is reminiscent of dilution only, which would suggest that zircon is absent above the solidus with essentially all of the Zr contained in the melt. As expected, Hf mimics the behaviour of Zr.

Thorium increases sharply above 850°C (LC) and 900°C (HC), before following a dilution path. Concentrations jump from <1 ppm to around 15 ppm, coinciding with the exhaustion of epidote in both lithologies. Epidote therefore appears to be the main host of Th in our experiments. Uranium shows a similar pattern to Th, but we note that there are other residual minerals that could co-host U in addition to epidotes (e.g. carbonate; Supplementary Data file SD 4).

The behaviour of the LREE in LC closely mimics Th, suggesting that LREE are also hosted by epidote. This is in accord with data on natural eclogites (e.g. El Korh *et al.*, 2009). There is an extreme increase in ΣLREE (La–Sm) from 5 to 160 ppm at the point of epidote exhaustion (850–900°C). At higher temperatures both epidote and carbonate (the other potential host of LREE) are absent, so the LREE become entirely incompatible. In HC, in contrast, ΣLREE steadily increases from ~4 ppm in the presence of epidote at 900°C to over 40 ppm at higher temperatures. This pattern reflects exhaustion of epidote followed by LREE control by carbonate at 1000°C (Supplementary Data file SD 4), and probably carbonatite melt at 1100°C. Yttrium + HREE show typical partitioning-controlled trends wherein concentrations strongly increase with increasing temperature, but absolute concentrations differ significantly depending on the residual garnet fraction and initial concentration. However, as only one HC experiment actually contains garnet (900°C) it is suggested that carbonate co-hosts the HREE and is additionally responsible for this pattern (Supplementary Data file SD 4).

Certain trace element ratios such as U/Th, Ba/Th and La/Sm$_{PUM}$ (where PUM indicates primitive upper mantle) are considered critical in the interpretation of subduction-zone processes (Fig. 7b). Melts from epidote-bearing experiments exhibit very high source-normalized U/Th values, which fall to unity only after epidote is exhausted. Barium/Th is extremely high (>5000) in one phengite-absent/epidote-present experiment (900°C, HC), and moderately high (~400) in a phengite- and epidote-bearing experiment (850°C, LC).
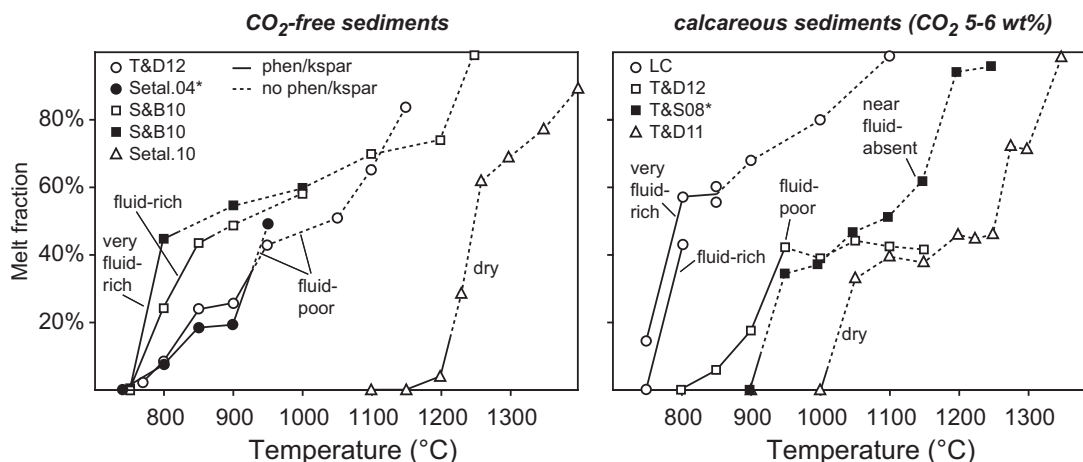
Fig. 8. Comparisons of melt productivity (melt fraction) as a function of temperature and fluid content in selected experiments on carbon-free and carbon-bearing sediments (calcareous sediments only). Initiation of melting in carbon-bearing sediments appears to be dependent on bulk H_2O/CO_2. Data sources: T&D12, Tsuno & Dasgupta (2012); Setal.04, Schmidt *et al.* (2004); S&B10, Skora & Blundy (2010); Setal.10, Spandler *et al.* (2010); T&S08, Thomsen & Schmidt (2008*a*); T&D11, Tsuno & Dasgupta (2011). Fluid-poor experiments had low bulk water contents (<2 wt %), fluid-rich experiments contained about 6–8 wt % H_2O, whereas the very fluid-rich experiments contained about 15–22 wt % H_2O. It should be noted that the experiments of Setal.04 and T&S08 were conducted at higher pressures and are projected to 3 GPa.

Epidote maintains low Th concentrations in coexisting melts, whereas Ba is most enriched in run products at the point of phengite exhaustion. High melt fraction, phengite- and epidote-free experiments have low Ba/Th (LC, 900–1100°C; Ba/Th $\approx$ 20–50). Epidote also maintains low LREE, whereas Sm is co-controlled by garnet. Thus La/Sm$_{PUM}$ (where PUM indicates primitive upper mantle) is low (close to unity) when residual epidote is present and highest (around 4–6) in epidote-free, garnet-bearing experiments. It should be noted that the HC, 900°C epidote-bearing experiment exhibits an unusually high variability in La/Sm$_{PUM}$ (5·9 $\pm$ 3·7), and is therefore ignored because it is not very meaningful.

DISCUSSION
Melting of calcareous sediments ($CO_2 \sim$ 5–6 wt %)
To explore the implications of our results for the fate of subducted calcareous sediments it is instructive to make comparisons with other experimental studies. In experiments on carbon-free sediments, the early stages of melting proceed through the breakdown of hydrous phases, essentially phengite (e.g. Schmidt *et al.*, 2004; Hermann & Spandler, 2008; Skora & Blundy, 2010) and/or biotite (e.g. Nichols *et al.*, 1994, 1996; Martindale *et al.*, 2013) at 3 GPa. The fluid-absent phengite dehydration reaction has been found to occur at 900–950°C at 3 GPa (Schmidt *et al.*, 2004), whereupon melting begins via the reaction

$$\text{Phengite} + \text{Quartz/Coesite} + \text{Clinopyroxene} = \text{Melt} + \text{Garnet.} \qquad (1)$$

In the fluid-present case, it has been shown that melting starts at temperatures of around 730–750°C at

3 GPa (e.g. Nichols *et al.*, 1994, 1996; Schmidt *et al.*, 2004; Hermann & Spandler, 2008; Skora & Blundy, 2010) through the reaction

$$\text{Phengite} + \text{Quartz/Coesite} + \text{Clinopyroxene} + H_2O = \text{Melt} \pm \text{Garnet} \pm \text{Kyanite.} \qquad (2)$$
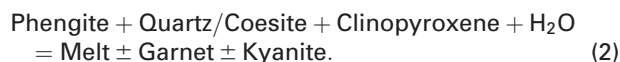
Melt production thereafter depends on the bulk water content. For low bulk water contents relatively little melting is required at the solidus to consume the fluid and large melt fractions are not reached until phengite itself breaks down via reaction (1) at higher temperatures. In contrast, at high water contents, a larger amount of melting occurs at the solidus via reaction (2), and phengite may disappear before the temperature of the peritectic-like phengite-out reaction (1) is reached (see figure 18 of Skora & Blundy, 2010). This difference in melting behaviour is illustrated in Figure 8.

For calcareous sediments at around 3 GPa Thomsen & Schmidt (2008*a*) located the fluid-absent solidus at 900–950°C, and indicated that phengite breakdown in the presence of carbonate is again responsible for significant production of potassium-rich granitic melt via the reaction

$$\text{Phengite} + \text{Quartz/Coesite} + \text{Clinopyroxene} + \text{Carbonate} = \text{Melt} + \text{Garnet} + \text{Kyanite.} \qquad (3)$$
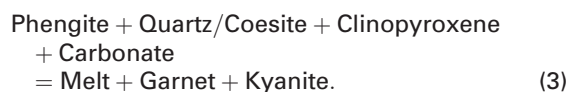
This is consistent with Mann & Schmidt (in press) who bracketed the fluid-absent solidus at 3 GPa to lie between 850–930°C. Thomsen & Schmidt (2008*a*) also reported miniscule menisci in some lower temperature runs, which were interpreted to represent silicate melt at fractions of <1%. Tsuno & Dasgupta (2012) identified a similar melting reaction, but K-feldspar also appeared in their near-solidus assemblage. Small degrees of melt were reported at 850°C in Tsuno & Dasgupta's

experiments, which had low bulk H_2O contents (1 wt %), but the production of significant amounts of melt was again restricted to $T > 900°C$.

In our LC experiments, the onset of melting depends on the bulk H_2O content. Melting starts at $760°C < T_{solidus} < 800°C$ in the experiment with 7·8 wt % H_2O, whereas some melt was already present at around $760°C$ in the experiment containing 15 wt % H_2O. Melting in the LC experiments is marked by the appearance of glass, garnet and kyanite at the expense of phengite, quartz/coesite, and clinopyroxene and minor carbonate. This suggests the melting reaction

$$\text{Phengite} + \text{Quartz/Coesite} + \text{Clinopyroxene}$$
$$+ \text{Carbonate} + H_2O$$
$$= \text{Melt} + \text{Garnet} + \text{Kyanite} \qquad (4)$$
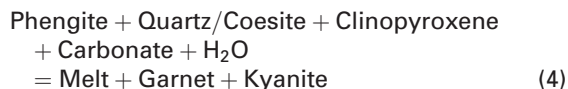
which is similar to the melting reaction inferred by Thomsen & Schmidt (2008*a*).

Thus it appears that the fluid-present experimental solidi obtained for various calcareous sediment compositions are much more variable, displaced up-temperature relative to the CO_2-free solidus by up to around 100°C (Fig. 8). One explanation for this displacement is that CO_2 lowers the activity of H_2O in the fluid phase and consequently raises the temperature of the fluid-saturated solidus. Based on thermodynamic models of pelite decarbonation (Kerrick & Connolly, 2001*b*), Thomsen & Schmidt (2008*a*) concluded that the CO_2 content of subsolidus fluids would be too low to significantly affect solidus temperatures. Consequently, they suggested that the experimentally determined solidus temperatures are overestimated in CO_2-bearing experiments, owing to the difficulty of identifying small melt fractions in run products that contained little H_2O. Although acknowledging that this explanation is plausible, we revisit the hypothesis that the subsolidus fluid composition may influence the onset of fluid-saturated melting. In particular, we suggest that in experiments with low bulk H_2O contents, the subsolidus fluids are more CO_2 rich than in the high bulk H_2O content experiments.

Modelling the onset of melting of calcareous sediments

Because we have no direct data on subsolidus fluid compositions, we model subsolidus fluid evolution by free energy minimization (Connolly, 1990). For this purpose we employ the thermodynamic dataset of Holland & Powell (1998) together with the solution models used by Kerrick & Connolly (2001*b*). As in the study of Kerrick & Connolly (2001*b*), we do not model the melt phase; however, this is immaterial as we are interested in the fluid composition at temperatures up to the onset of melting. For each composition used in the calculations there is a solidus somewhere in the modelled temperature range, above which the predicted phase relations are metastable with respect to melt-bearing assemblages (including fluid X_{H2O}). Experimentally,

solidus temperatures lie between 730–750°C (H_2O-saturated, CO_2-free system) and 900–950°C (fluid-absent) at 3 GPa.

We model the following compositions: LC (bulk $CO_2 = 6$ wt %) with a range of bulk H_2O contents (1, 6 and 22 wt %); HC ($CO_2 = 16$ wt %; $H_2O = 22$ wt %); the experimental starting materials of Thomsen & Schmidt (2008*a*) ($CO_2 = 4·8$ wt %; $H_2O = 1$ wt %) and Tsuno & Dasgupta (2012) ($CO_2 = 5$ wt %; $H_2O = 1$ wt %). It was necessary to slightly augment the H_2O content given by Thomsen & Schmidt (2008*a*) (to 1·39 wt %) because the calculated phase assemblages were below fluid-saturation, inconsistent with their experimental observations. Results including the fluid fraction F, fluid X_{H2O}, and the modal proportions by weight of phengite and solid carbonate are presented in Fig. 9, with full details given in Supplementary Data file SD 5. Fluid, phengite, carbonate, omphacite, garnet and quartz/coesite $\pm$ kyanite are present in all calculations, consistent with the results of our subsolidus experiment. The further indication from Fig. 9 is that the temperature of phengite breakdown is sensitive to water activity and, therefore, the bulk water content, as discussed by Clemens & Vielzeuf (1987). The presence of alkali feldspar, as a replacement for phengite as the K_2O-bearing phase at the highest modelled temperatures, is an artefact of our calculations, which lack a melt phase to accept potassium after phengite breakdown.

Over our range of bulk compositions the minimum value of fluid X_{H2O} coexisting with silicates and carbonate is $\sim 0·2–0·3$, calculated for the bulk composition of Thomsen & Schmidt (2008*a*) and the LC composition with $H_2O \ll CO_2$ at 850°C; the maximum is $\sim 0·9$, calculated for the LC composition with $H_2O \gg CO_2$ (Fig. 9). Calculated X_{H2O} is correlated with experimental solidus temperatures for calcareous sediments (Fig. 10). Absolute values of fluid X_{H2O} should be treated with caution because of uncertainties in the activity–composition relations under conditions at which the fluid would have a significant dissolved silicate component. However, the uncertainties will be systematic in nature, such that the relative fluid compositions at subsolidus conditions should be relevant to the experiments (and to nature).

Our results imply that the near-solidus fluid can show a much greater range of fluid X_{H2O} than could be anticipated from the calculations of Kerrick & Connolly (2001*b*), using the same thermodynamic models. This variability may account for the range of experimental solidus temperatures for calcareous sediments. In particular, for bulk compositions with non-trivial CO_2/H_2O contents, significant decarbonation occurs immediately above the temperature of the H_2O-saturated solidus (Fig. 9), leading to a large divergence in the X_{H2O} of the fluid phase and likewise in $T_{solidus}$. In Fig. 10 we show that the relationship between experimental $T_{solidus}$ and calculated X_{H2O} in calcareous sediments is similar to that found in the systems albite–H_2O–CO_2 at
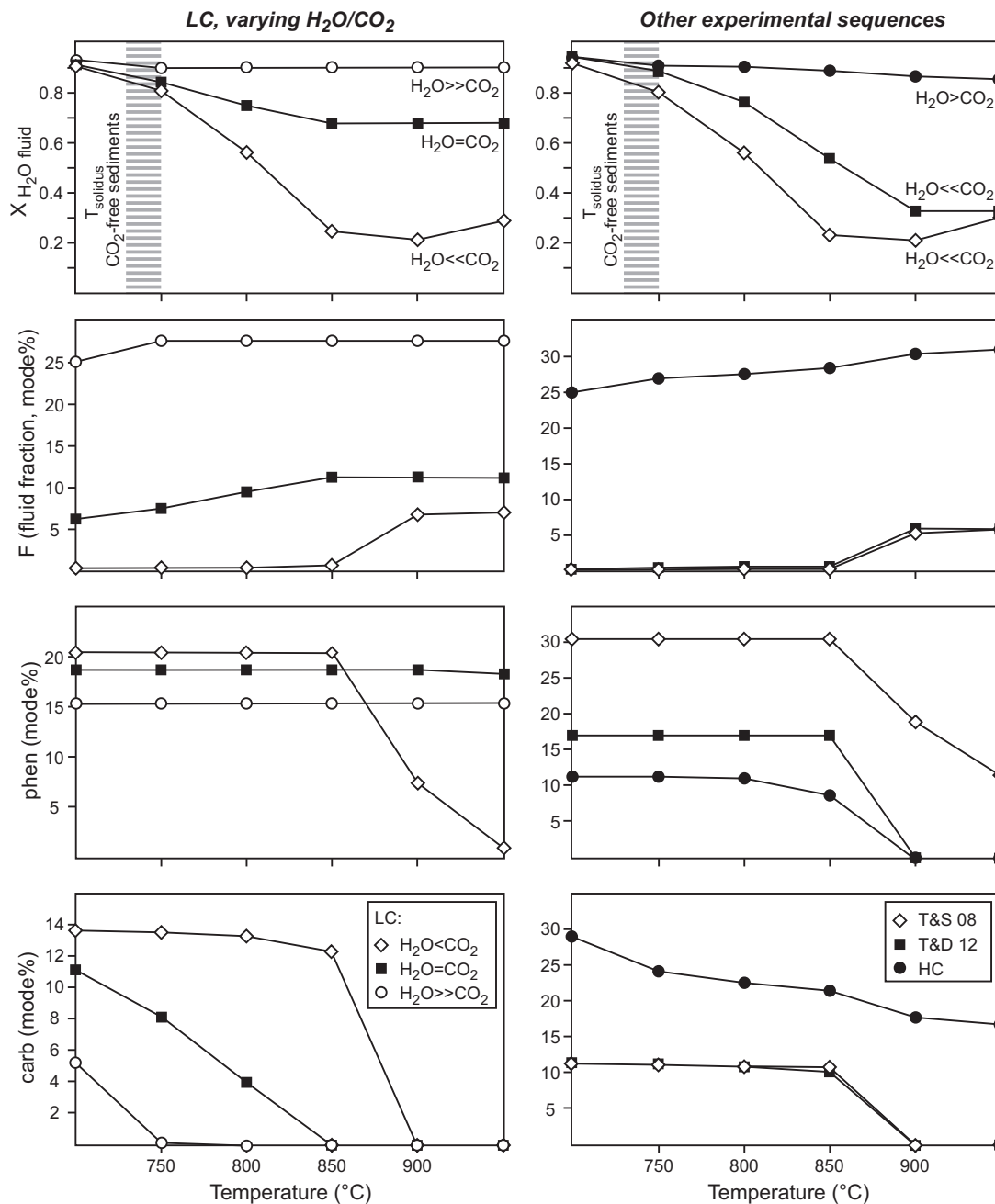
Fig. 9. Calculated fluid X_{H2O}, fluid fraction F, and modal % by weight of phengite and carbonate using Perple_X. The modelled bulk composition is our LC lithology in one set of calculations, with fixed CO_2 (6 wt %) and variable H_2O (1, 6 or 22 wt %). The other set of calculations uses the actual bulk compositions of the various experimental studies (T&S 08, Thomsen & Schmidt, 2008*a*; T&D 12, Tsuno & Dasgupta, 2012). The changing phengite and carbonate modal percentages are correlated with changes in fluid X_{H2O} and F at $T \geq 700°C$. By 750°C, the temperature at which melt would be expected to occur in carbon-free sediments, fluid X_{H2O} in the different bulk compositions starts to diverge significantly. The calculations suggest that $T_{solidus}$ should be variable in carbon-bearing sediments, being lowest in bulk compositions that have high H_2O/CO_2 ratios. (Note that in the labelling of the curves in the left-hand panel, the values of H_2O and CO_2 are in wt %, so the condition $H_2O = CO_2$ is not thermodynamically significant.)

1·5–2·0 GPa (Bohlen *et al.*, 1982) and haplogranite–H_2O–CO_2 at 1·5 GPa (Keppler, 1989). We conclude that fluid X_{H2O} just below the solidus in calcareous sediments is sensitive to bulk H_2O, CO_2 and K_2O, the last of these controlling the maximum modal proportion of phengite, and is not simply buffered to high X_{H2O} by the co-existence of carbonate, hydrous and silicate minerals.

Applications to nature

In applying the ideas above to the onset of melting of calcareous sediments we must recognize the difference between the open-system environment that might be expected in subduction zones and the closed-system environment of the experiments and calculations of this study and those of Kerrick & Connolly (2001*b*). If
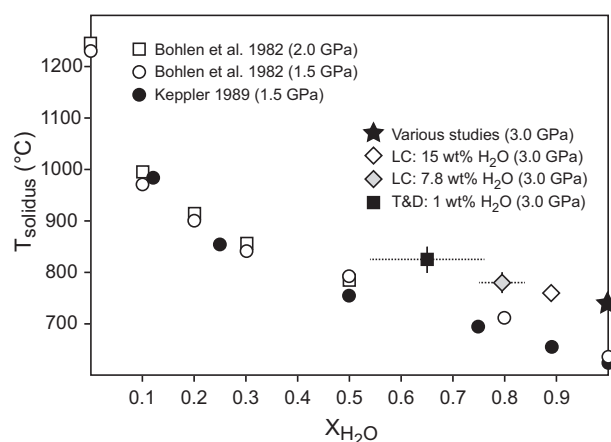
Fig. 10. Variation of $T_{solidus}$ vs fluid X_{H_2O} for various experimental sequences. The data of Bohlen *et al.* (1982) and Keppler (1989) were obtained in simple systems (albite–H_2O–CO_2 and albite–K-feldspar–H_2O–CO_2) at pressures of 1·5–2·0 GPa. The 3·0 GPa data are taken from several experimental studies. The $T_{solidus}$ in the CO_2-free system (black star) was well determined to be at around 730–750°C at 3·0 GPa by Nichols *et al.* (1994, 1996), Schmidt *et al.* (2004), Hermann & Spandler (2008) and Skora & Blundy (2010). Grey and white diamonds represent the melting behaviour of LC with 7·8 and 15 wt % H_2O respectively; the black square represents the experiments reported by Tsuno & Dasgupta (2012). [The experiments of Thomsen & Schmidt (2008*a*) are not plotted because the fluid-saturated solidus of their study is not well constrained.] Uncertainties in $T_{solidus}$ represent the limits in precision with which the fluid-saturated solidus has been bracketed. Uncertainties in calculated fluid X_{H_2O} values reflect the range of fluid composition modelled with Perple_X within the experimental temperature uncertainty. These are minimum uncertainties, as they do not include any potential inaccuracy in the modelling. The figure nevertheless implies that the observed differences in $T_{solidus}$ in 3·0 GPa experiments can be attributed to variable fluid X_{H_2O} conditions, and that the net effect of fluid X_{H_2O} on $T_{solidus}$ is roughly comparable with experiments performed in simple systems.

unlimited fluid of constant X_{H_2O} can be supplied to the subducting sediment layer through the dehydration of underlying lithologies (an 'external buffering' scenario), then it is this imposed fluid composition that will control phase equilibria, including solidus temperature, regardless of whatever fluid evolution would have occurred in a closed system. Should the externally buffering fluid be of high X_{H_2O} (most closely approximated by our LC experiments), melting might be expected to begin at temperatures that are only slightly above the H_2O-present solidus of carbonate-free sediments. Melt productivity would be maximized and significant amounts of melt could be generated if slab-top temperatures were as high as 750–800°C (e.g. Van Keken *et al.*, 2002) (Fig. 11); this has implications both for the recycling of sedimentary carbonate to greater mantle depths and the supply of CO_2 to the mantle wedge. External buffering to a lower fluid X_{H_2O} would dictate somewhat higher solidus temperatures and lower melt productivities. We acknowledge, however, that the natural system is also likely to be open with respect to melt and to fluid-mobile elements, and furthermore that any realistic analysis should take this into account.

Phase assemblages and melting behaviour of marls—preliminary results

The interpretation of our HC (marl) experiments is complicated because the final fO_2 is unknown, and there is no other study available on similar compositions with which we can compare our results. We can thus only speculate about the significance of our HC phase assemblages and $T_{solidus}$. One of the most striking observations is that garnet is absent at 800–900°C. The presence or absence of garnet is likely to be a complex function of the bulk-rock composition, including Fe_2O_3. Any system in which a significant fraction of iron is present as Fe_2O_3 will have a high bulk Mg# approaching unity, and resulting phase assemblages might be comparable with experiments that were performed in Fe-free model compositions. Indeed, garnets in KCMASH (e.g. Hermann, 2002) appear at $T \approx 900$°C at 3 GPa, whereas in Fe^{2+}-bearing compositions garnet is present at $T = 700$°C (e.g. Hermann & Spandler, 2008). Garnet also appears at $T \approx 1000$°C at 3 GPa in the KCMASH-CO_2 experimental study of Thomsen & Schmidt (2008*b*), consistent with the temperature of garnet-in of our study. We thus speculate that the presence or absence of garnet is linked to the high bulk Fe_2O_3.

Regardless of the differences in garnet stability, it appears that melting of marls is initiated by the same melting reaction as in calcareous sediments [reaction (4)] in terms of reactants, except that epidote is produced instead of garnet:

$$\text{Phengite} + SiO_2 + \text{Clinopyroxene} + \text{Carbonate} + H_2O$$
$$= \text{Melt} + \text{Epidote}.$$

$$(5)$$
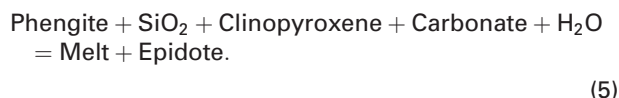
Although melt is present at 800°C, its abundance is very low. This suggests that melting of HC started at temperatures close to 800°C, despite the presence of significant amounts of excess water (>20 wt %). This is in contrast to the LC experiments, where melting started close to 760°C and melt was abundant at 800°C (40–60%). Whether the presence of abundant Fe_2O_3 lowers or increases $T_{solidus}$ is not well known at present. Comparing the melting behaviour of Fe-free model systems with Fe^{2+}-bearing compositions would suggest that the bulk-rock compositions with high Mg# should melt at higher temperatures, although in the case of sediments this requires there to be a host for significant Fe_2O_3 in the solid residue. It is striking that almost all experimental studies on natural sediments have constrained the fluid-present solidus at 3 GPa to be at around 730–750°C. One prominent exception is the experimental sequence of Johnson & Plank (1999), who melted natural ferric-iron-rich red clay at 3 GPa. Those researchers constrained the fluid-present solidus to be at 830°C. Their experimental run products are consistent with a high bulk ferric-iron content; for example, ilmenite–hematite is present, which is not the case in other melting experiments on sediments that contain rutile (± ilmenite–hematite) (e.g. Schmidt *et al.*, 2004;
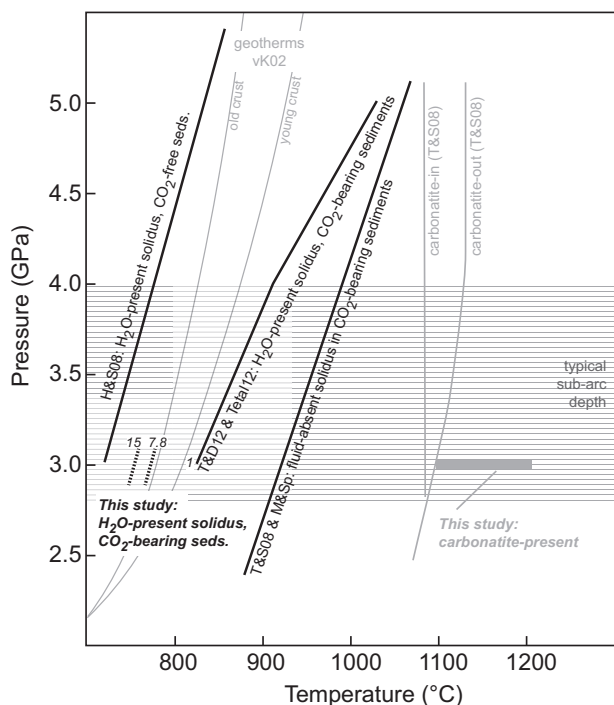
Fig. 11. Summary of different sediment solidi (carbon-bearing and carbon-free) and representative geotherms for subduction-zone environments. Carbon-bearing sediments are shown to plausibly melt at temperatures thought to prevail at sub-arc depths. Data sources: H&S08, Hermann & Spandler (2008); vK02, Van Keken *et al.* (2002); T&D12, Tsuno & Dasgupta (2012); Tetal12, Tsuno *et al.* (2012); T&S08, Thomsen & Schmidt (2008*a*); M&Sp, Mann & Schmidt (in press).

Hermann & Spandler, 2008; Skora & Blundy, 2010). This would be consistent with our speculation that melting in ferric-iron-rich systems starts at higher temperatures, and that ferric iron is compatible in the solid assemblage at 3 GPa (e.g. ilmenite–hematite, epidote). We thus speculate that more melt would have been present, alongside garnet, in the HC experiments if conditions were more reduced. Conversely, assuming that some of the ferric iron became reduced in the course of the experiments (consistent with the presence of ferrous iron in carbonate, for example), it is also possible that marls even richer in Fe_2O_3 would melt at even higher temperatures.

CO_2 recycling in subduction zones

The efficacy of calcareous sediment-derived melts in delivering CO_2 to the mantle wedge depends on the degree of melting and the solubility of CO_2 in silicate melts and coexisting fluid at sub-arc depths. Experimental studies to date suggest that calcareous sediments behave in a refractory manner under 'normal' subduction-zone conditions if the availability of water is limited (e.g. Thomsen & Schmidt, 2008*a*, 2008*b*; Tsuno & Dasgupta, 2011, 2012; Tsuno *et al.*, 2012; Mann & Schmidt (in press)). In contrast, our experiments show that H_2O-fluxed melting of calcareous sediments can result in very large melt fractions (>50%), even at near-

solidus temperatures of only 750–800°C at 3 GPa. This melt has the potential to carry appreciable CO_2, although the solubility of CO_2 in sediment partial melts is not well constrained at present. The solubility of CO_2 in anhydrous, broadly granitic melts at 3 GPa is probably of the order of 1·6–1·9 wt % (e.g. Fine & Stolper, 1985; Duncan & Dasgupta, 2014; see also Supplementary Data file SD 6). The solubility of CO_2 can be further enhanced in the presence of H_2O in high-pressure melts (e.g. Mysen, 1976; King & Holloway, 2002; Duncan & Dasgupta, 2014). Unfortunately, the latter studies are all limited to low H_2O contents (<4 wt %) that are well below those expected in near-solidus partial melts (H_2O ~20–30 wt %; see, e.g. Kessel *et al.*, 2005; Hermann *et al.*, 2006; Hermann & Spandler, 2008). We attempted to measure CO_2 solubility in our experimental run products using secondary ion mass spectrometry, but encountered a suite of problems related to the high overall volatile contents and the lack of appropriate standards. Our preliminary data (provided in Supplementary Data file SD 6) suggest that although the exact CO_2 solubility at sub-arc conditions remains unknown for a flush-melting event, there is the possibility that CO_2 is significantly more enriched than the CO_2 concentrations of even the most water-rich experiments of Duncan & Dasgupta (2014).

In the absence of CO_2 solubility data at H_2O-rich conditions, our results can still place useful constraints on large-scale carbon cycles, because we can use mass balance to reconstruct how much of the bulk carbon remains stable in the solid residue after melt and fluid extraction. Table 7 shows that carbonate-poor lithologies, such as LC ($CO_2 = 6.1$ wt %) retain as little as 20–35% of their initial carbon inventory in the form of residual carbonate at 750–850°C. At similar temperatures carbonate-rich lithologies (HC; $CO_2 = 16.2$ wt %) will transfer around 70% of their carbon inventory to the Earth's deep interior. These results can be used to place maximum constraints on the return flux of CO_2 from subducted sediments in arc volcanoes. Burton *et al.* (2013) estimated global subaerial volcanic CO_2 emissions to be as high as 540 Mt a^{-1}, from which 60–80% is probably related to arc volcanism (M. R. Burton, personal communication). Plank & Langmuir (1998) estimated that the influx of CO_2 via global subducting sediments (GLOSS) is ~40 Mt a^{-1}. If the majority of this carbon were subducted in calcareous clay (LC), which is very similar to the GLOSS composition, then we can assume that about 65–80% of the subducted carbon (26–32 Mt a^{-1}) can be returned to the Earth's surface, provided that abundant excess water is available for decarbonation and melting of the slab at 750–850°C. These values must be regarded as a benchmark for the maximum possible return flux of sediment-derived CO_2 for various reasons. First, they assume that CO_2 is evenly distributed throughout subducted sediments worldwide. In reality, carbonate subduction is restricted to relatively few arcs, and in consequence it is clear that some of the carbonate inventory must be subducted as

Table 7: CO_2 budgets ($P = 3$ GPa)

Run	T (°C)	$CO_{2\,ini}$ (wt %)	carb %	carb 1σ	$CO_{2\,s}$ (wt %)	$CO_{2\,s}$ 1σ	$CO_{2\,liq}$ (wt %)	$CO_{2\,liq}$ 1σ	% CO_2 arcs	% CO_2 earth
Carbonate-rich lithology										
144-16-c6	900	16·2	25	1	11	1	5	1	32	68
144-16-c7	1000	16·2	19·1	0·8	8·4	0·3	7·8	0·3	48	52
144-16-c14	1000	16·2	22·2	0·9	9·8	0·4	6·4	0·4	40	60
144-16-c18	1100	16·2	6·3	0·6	2·8	0·3	13·4	0·3	83	17
144-16-c16	1200	16·2	0·0	0·0	0·0	0·0	16·2	0·1	100	0
Carbonate-poor lithology										
144-38-c35	750	6·1	4·8	1·0	2·1	0·4	4·0	0·4	65	35
144-38-c34	750	6·1	3·9	1·0	1·7	0·4	4·4	0·4	72	28
144-38-c28	800	6·1	4·8	0·7	2·1	0·3	4·0	0·3	65	35
144-38-c29	800	6·1	3·8	0·5	1·7	0·2	4·4	0·2	73	27
144-38-c4	850	6·1	2·5	1·0	1·1	0·4	5·0	0·4	82	18
144-38-c15	850	6·1	2·6	0·9	1·1	0·4	5·0	0·4	81	19
144-38-c11	900	6·1	0·0	0·0	0·0	0·0	6·1	0·0	100	0
144-38-c13	1000	6·1	0·0	0·0	0·0	0·0	6·1	0·0	100	0
144-38-c19	1100	6·1	0·0	0·0	0·0	0·0	6·1	0·0	100	0

carb, carbonate; $CO_{2\,s}$, calc. CO_2 in bulk solid residue; $CO_{2\,liq}$, CO_2 in bulk liquids (melt and second vapour phase); % CO_2 arcs, % CO_2 that is returned in arcs; % CO_2 Earth, % CO_2 that is recycled into the deep Earth interior.

marl (HC) or even pure limestone layers (see also Fig. 1), which will retain more carbonate compared with calcareous clay. For example, if the majority of the carbon in GLOSS was subducted as marl (HC) only about 30% of the subducted CO_2 (12 Mt a^{-1}) could be returned. In addition, the calculations assume pervasive infiltration of H_2O, whereas in nature water infiltration might be highly channelized (e.g. John *et al.*, 2008), and carbon could be extracted efficiently only from those areas that have high fluid–rock ratios at 750–850°C. Lastly, the calculations presume that no sediment is scraped off during subduction and that there is no further precipitation of solid carbonate in the mantle wedge (e.g. at the cold slab–mantle interface) or at the Moho. We also recognize that the flux of CO_2 from slab to arc volcanism may be modulated by long-term storage in deep crustal hot zones, such that the annual influx does not always balance the annual efflux on timescales that are short relative to storage timescales.

Trace element signature of slab-derived partial melts

The trace element signatures of partial melts in calcareous sediments bear many similarities to those of carbon-free lithologies (e.g. Johnson & Plank, 1999; Hermann & Rubatto, 2009; Skora & Blundy, 2010, 2012). For example, partial melts are enriched in the typical 'fluid-mobile' elements such Cs, Ba, Rb and K; Sr is also enriched and has comparable absolute concentrations with those in the studies cited above. The fact that Sr is partly retained in carbonates is compensated by higher initial Sr contents. Zirconium (and Hf) is relatively enriched (of the order of 100 ppm), in agreement with Rubatto & Hermann (2007). Titanium, Nb, and Ta are depleted (e.g. Pearce & Cann, 1973; McCulloch & Gamble, 1991; Hawkesworth *et al.*, 1993; Thirlwall *et al.*, 1994), owing to retention in residual rutile until about 1000°C. Heavy REE + Y are low in partial melts,

consistent with their compatibility in residual garnet. The control of residual phases on trace elements in sediment partial melts has been further discussed by Hermann & Rubatto (2009) and Skora & Blundy (2010, 2012). A new finding is the observation that significant quantities of HREE may also be retained by residual carbonate even in the absence of garnet, as shown for the HC experiments at $T < 1000$°C.

Light REE, Th and U patterns differ somewhat from those previously reported; for example, in the experiments of Hermann & Rubatto (2009) and Skora & Blundy (2010, 2012). In these carbon-free, Ca-poor sediments, monazite solubility controls LREE, Th and U concentrations in partial melts. In our experiments on calcareous sediments it is epidote ± carbonate that control LREE + Th concentrations in melts and these remain low (ppm to sub-ppm level) until 900–1000°C when epidote and carbonate are exhausted from the residue. In our epidote-free, but carbonate-present experiments at 1000–1100°C, ΣLREE in partial melts is of the order of 40–70 ppm, representing ~65–75% of the initial inventory. The importance of epidote is consistent with the study of Carter *et al.* (in preparation), who found that in undoped mid-ocean ridge basalt (MORB) and altered oceanic crust (AOC), epidote (and not allanite; see Klimm *et al.*, 2008) is the LREE-controlling phase even above the solidus, suppressing ΣLREE concentrations to very low values. In fact, epidote retains ΣLREE to such high degrees that the Nb/La ratio in the melt is greater than that of PUM under all conditions where epidote is present in the solid residue. It should be noted, however, that mixing in even tiny amounts of partial melts derived from epidote-free sources, such as radiolarian clay (Skora & Blundy, 2010), would be sufficient to restore the arc-typical Nb anomaly in the bulk fluid composition, simply because of the predominance of LREE in partial melts in the absence of epidote. Likewise, a more Ti-rich protolith would have higher residual rutile at all temperatures and consequently have

lower Nb/La ratios than the partial melts produced in this study.

Another important difference is the fact that partial melts in equilibrium with epidote + phengite have much higher Ba/Th compared with partial melts in equilibrium with monazite + phengite (Hermann & Rubatto, 2009; Skora & Blundy, 2010, 2012). This ratio is maximized when phengite, the principal host for Ba, is exhausted but epidote, the principal host for Th, persists. Elevated Ba/Th ratios were originally interpreted as a geochemical characteristic of fluids originating from AOC or MORB in the three-component model (AOC fluid, sediment melt, mantle melt) of Elliott (2003). Subsequent experimental studies have shown that indeed MORB-derived partial melts do satisfy these criteria, mainly because residual epidote serves to increase Ba/Th by holding back Th and reduce La/Sm$_{PUM}$ by REE fractionation (Carter *et al.*, in preparation). Residual allanite (= LREE-epidote) would create a very similar geochemical pattern (Hermann, 2002; Klimm *et al.*, 2008). Conversely, residual zoisite in the slab cannot explain low La/Sm$_{PUM}$ (Martin *et al.*, 2011) because REE partitioning into the various epidote-group minerals depends on crystal chemistry and structure (e.g. Frei *et al.*, 2003), and zoisite prefers the middle REE (MREE) instead of LREE. Our study suggests that, in some cases, partial melts derived from calcareous sediments may masquerade as an AOC-derived component in terms of their elevated Ba/Th and low La/Sm$_{PUM}$ ratios, owing to the presence of residual epidote (Fig. 12). Figure 12 also shows that although Ba/Th ratios in melts of calcareous sediments are elevated, they cannot explain Ba/Th values of arc lavas that exceed 1000. For these an 'AOC fluid source' is still required (Carter *et al.*, in preparation). In the Lesser Antilles arc, where sediment subduction is commonplace, lava chemistry could be potentially explained by mixing of partial melts derived from epidote-rich sediments on the one hand (Ba/Th ∼ 400 and La/Sm$_{PUM}$ ∼ 1) and epidote-poor or epidote-free clastic sediments on the other hand (Ba/Th < 100 and La/Sm$_{PUM}$ > 5) (Fig. 12), although MORB-derived fluids may, of course, also contribute to the arc signal. In any case, the Ba/Th vs La/Sm$_{PUM}$ diagram of Elliott (2003) is better interpreted in terms of residual phases in the slab rather than source lithology: phengite reduces Ba/Th, and epidote and monazite increase Ba/Th; epidote reduces La/Sm$_{PUM}$; garnet and carbonate increase La/Sm$_{PUM}$.

Epidote fractionates U from Th such that partial melts will have excess in U when compared with bulk U/Th. The same fractionation trend was previously observed for allanite in the doped-MORB experiments of Klimm *et al.* (2008). Worldwide, it has been found that lavas from sediment-poor arcs exhibit a [238]U excess over [230]Th relative to their source, in contrast to sediment-rich arcs, which appear to plot close to the ([238]U/[232]Th) vs ([230]Th/[232]Th) equiline, or even towards Th excess (e.g. McDermott & Hawkesworth, 1991; Condomines & Sigmarsson, 1993); a recent appraisal of
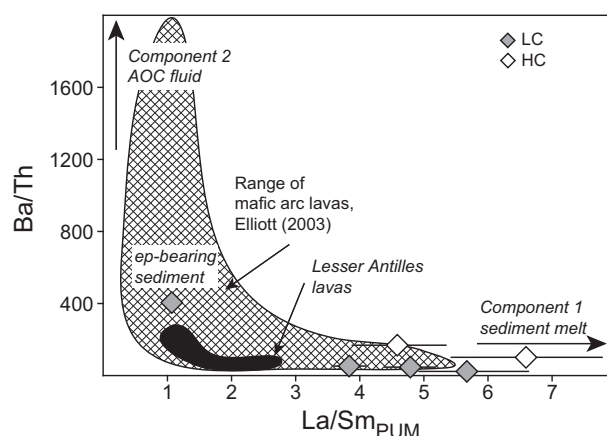

Fig. 12. PUM-normalized La/Sm$_{PUM}$ vs Ba/Th variations for mafic arc lavas worldwide [compilation of Elliott (2003)]. Superimposed are the chemical compositions of quenched glasses from this study. High Ba/Th ratios coupled with low La/Sm$_{PUM}$ are observed in epidote-bearing experiments, and are otherwise restricted to fluids or melts coming from the basaltic portion of the subducted slab. The Lesser Antilles arc lavas trace element signature could be explained by mixing of partial melts derived from epidote-rich sediments (Ba/Th ∼ 400 and La/Sm$_{PUM}$ ∼ 1) and epidote-poor or epidote-free sediments (Ba/Th < 100 and La/Sm$_{PUM}$ > 5).

these variations in the context of residual mineralogy has been given by Avanzinelli *et al.* (2012). Again, although U excesses are generally seen as a fingerprint of the fluid or melt that stems from the basaltic portion of the subducted slab, calcareous sediments may also provide such a signature.

Evidence for oxidized slabs and epidote in UHP rocks

As our experimental run products record the ultrahigh-pressure (UHP) phase petrology of oxidized sediments it is reasonable to ask whether the presence of epidote is directly linked to the oxidizing conditions (high bulk Fe^{3+}/Fe^{tot}), and whether such oxidized conditions can be identified in fossil UHP terrains. Marine sediments are known to vary greatly in their Fe^{3+}/Fe^{tot}, which can be very high (>0·9) locally. At present, it is not clear whether a high ferric iron component can be maintained in the slab, or whether ferric iron would react with reduced species to form ferrous iron (e.g. Lecuyer & Ricard, 1999).

Known occurrences of UHP epidote include, for example, the Western Alps (e.g. Reinecke, 1998; Compagnoni & Rolfo, 1999) and Dabie–Sulu (e.g. Rolfo *et al.*, 2004; Ferrando *et al.*, 2005; Zhang *et al.*, 2009). UHP epidotes are particularly common in Dabie–Sulu eclogites, which are well known for their oxidizing conditions. Studies on stable isotopes combined with petrological evidence have suggested that this area probably experienced pervasive hydrothermal alteration in an oxidized environment prior to UHP metamorphism (e.g. Zheng *et al.*, 2003).

It is unlikely that epidote will be stable in Ca-poor metapelites at UHP conditions, but there is some

evidence that epidote can be stable in UHP calc-silicates or impure marbles. For example, epidote is reported in the UHP calc-schists at Lago di Cignana, especially in formerly oxidized and Mn-rich layers (Reinecke, 1998; Compagnoni & Rolfo, 1999). Impure marbles from the Sulu terrain also contain abundant epidote, which has mainly grown during early retrograde stages at eclogite-facies conditions (e.g. Proyer *et al.*, 2014). However, the authors also suggested that 'the assemblage omphacite + garnet + quartz/coesite + epidote (rich in Fe^{3+} and REE) + rutile $\pm$ talc was passive during metamorphic evolution through the eclogite facies, perhaps to UHP conditions and back'. Such an assemblage, in addition to carbonate, is fully consistent with our experimental phase assemblages, suggesting that epidote can be stable at UHP conditions in oxidized bulk compositions, including carbonate-rich lithologies, and that initially oxidizing conditions can be maintained when the slab undergoes UHP metamorphism.

SUPPLEMENTARY DATA

Supplementary data for this paper are available at *Journal of Petrology* online.

REFERENCES

Adam, J., Green, T. H., Sie, S. H. & Ryan, C. G. (1997). Trace element partitioning between aqueous fluids, silicate melts and minerals. *European Journal of Mineralogy* **9**, 569–584.

Alt, J. C. & Teagle, D. A. H. (1999). The uptake of carbon during alteration of ocean crust. *Geochimica et Cosmochimica Acta* **63**, 1527–1535.

Alt, J. C., Honnorez, J., Laverne, C. & Emmerman, R. (1986). Hydrothermal alteration of a 1 km section through the upper oceanic crust, Deep Sea Drilling Project Hole 504B: mineralogy, chemistry and evolution of seawater–basalt interactions. *Journal of Geophysical Research* **91**, 10309–10335.

Avanzinelli, R., Prytulak, J., Skora, S., Heumann, A., Koetsier, G. & Elliott, T. (2012). Combined $^{238}U–^{230}Th$ and $^{235}U–^{231}Pa$ constraints on the transport of slab-derived material beneath the Mariana Islands. *Geochimica et Cosmochimica Acta* **92**, 308–328.

Bebout, G. E., Ryan, J. G., Leeman, W. P. & Bebout, A. E. (1999). Fractionation of trace elements by subduction-zone metamorphism—effect of convergent-margin thermal evolution. *Earth and Planetary Science Letters* **171**, 63–81.

Blundy, J. D. & Dalton, J. A. (2000). An experimental comparison of clinopyroxene–melt partitioning in silicate and carbonate systems and implications for mantle metasomatism. *Contributions to Mineralogy and Petrology* **139**, 356–371.

Blundy, J. D., Cashman, K. V., Rust, A. C. & Witham, F. (2010). A case for CO_2-rich arc magmas. *Earth and Planetary Science Letters* **290**, 289–301.

Bohlen, S. R., Boettcher, A. L. & Wall, V. J. (1982). The system albite–H2O–CO₂: a model for melting and activities of water at high pressures. *American Mineralogist* **67**, 451–462.

Bose, K. & Ganguly, J. (1995). Quartz–coesite transition revisited: Reversed experimental determination at 500–1200°C and retrieved thermochemical properties. *American Mineralogist* **80**, 231–238.

Brooker, R. A. & Kjarsgaard, B. A. (2011). Liquid immiscibility and phase relations in the system SiO₂–Na₂O–Al₂O₃–CaO–CO₂ at 0·1–2·5 GPa with applications to carbonatite genesis. *Journal of Petrology* **52**, 1281–1305.

Burton, M. R., Sawyer, G. M. & Granieri, D. (2013). Deep carbon emissions from volcanoes. In: Hazen, R. M., Jones, A. P. & Baross, J. A. (eds) *Carbon in Earth. Mineralogical Society of America and Geochemical Society, Reviews in Mineralogy and Geochemistry* **75**, 323–354.

Caldeira, K. (1992). Enhanced Cenozoic chemical weathering and the subduction of pelagic carbonate. *Nature* **357**, 578–581.

Carpentier, M., Chauvel, C. & Mattielli, N. (2008). Pb–Nd isotopic constraints on sedimentary input in the Lesser Antilles arc system. *Earth and Planetary Science Letters* **272**, 199–211.

Carpentier, M., Chauvel, C., Maury, R. & Mattielli, N. (2009). The 'zircon effect' as recorded by the chemical and Hf isotopic compositions of the Lesser Antilles forearc sediments. *Earth and Planetary Science Letters* **287**, 86–99.

Chopin, C. (1984). Coesite and pure pyrope in high-grade blueschists of the western Alps: a first record and some consequences. *Contributions to Mineralogy and Petrology* **86**, 107–118.

Clemens, J. D. & Vielzeuf, D. (1987). Constraints on melting and magma production in the crust. *Earth and Planetary Science Letters* **86**, 287–306.

Compagnoni, R. & Rolfo, F. (1999). Characteristics of UHP pelites, gneisses, and other unusual rocks. *International Geology Review* **41**, 552–570.

Condomines, M. & Sigmarsson, O. (1993). Why are so many arc magmas close to $^{238}U–^{230}Th$ radioactive equilibrium? *Geochimica et Cosmochimica Acta* **57**, 4491–4497.

Connolly, J. A. D. (1990). Multivariable phase-diagrams—an algorithm based on generalized thermodynamics. *American Journal of Science* **290**, 666–718.

Connolly, J. A. D. (2005). Computation of phase equilibria by linear programming: A tool for geodynamic modeling and its application to subduction zone decarbonation. *Earth and Planetary Science Letters* **236**, 524–541.

Connolly, J. A. D. & Cesare, B. (1993). C–O–H–S fluid composition and oxygen fugacity in graphitic metapelites. *Journal of Petrology* **11**, 379–388.

Cooper, L. B., Ruscitto, D. M., Plank, T., Wallace, P. J., Syracuse, E. M. & Manning, C. E. (2012). Global variations in H_2O/Ce: 1. Slab surface temperatures beneath volcanic arcs. *Geochemistry, Geophysics, Geosystems* **13**, doi:10.1029/2011GC003902.

Dasgupta, R. (2013). Ingassing, storage, and outgassing of terrestrial carbon through geologic time. In: Hazen, R. M., Jones, A. P. & Baross, J. A. (eds) *Carbon in Earth. Mineralogical Society of America and Geochemical Society, Reviews in Mineralogy and Geochemistry* **75**, 323–354.

Dasgupta, R. & Hirschmann, M. M. (2010). The deep carbon cycle and melting in Earth's interior. *Earth and Planetary Science Letters (Frontiers)* **298**, 1–13.

De Leeuw, G. A. M., Hilton, D. R., Fischer, T. P. & Walker, J. A. (2007). The He–CO_2 isotope and relative abundance characteristics of geothermal fluids in El Salvador and Honduras: New constraints on volatile mass balance of the Central American Volcanic Arc. *Earth and Planetary Science Letters* **258**, 132–146.

Domanik, K. J. & Holloway, J. R. (2000). Experimental synthesis and phase relations of phengitic muscovite from 6·5–11 GPa in a calcareous metapelite from the Dabie Mountains, China. *Lithos* **52**, 51–77.

Droop, G. T. R. (1987). A general equation for estimating Fe^{3+} concentrations in ferromagnesian silicates and oxides from microprobe analyses, using stoichiometric criteria. *Mineralogical Magazine* **51**, 431–435.

Duncan, M. S. & Dasgupta, R. (2014). CO_2 solubility and speciation in rhyolitic sediment partial melts at 1·5–3·0 GPa—Implications for carbon flux in subduction zones. *Geochimica et Cosmochimica Acta* **124**, 328–347.

Dungan, M., Rhodes, J., Long, P., Blanehard, D., Brannon, J. & Rodgers, K. (1979). Petrology and geochemistry of basalts from Site 396, Legs 45 and 46. *Initial Reports of the Deep Sea Drilling Project* **46**, 89–113.

El Korh, A., Schmidt, S. Th., Ulianov, A. & Potel, S. (2009). Trace element partitioning in HP–LT metamorphic assemblages during subduction-related metamorphism, Ile de Groix, France: a detailed LA-ICP-MS study. *Journal of Petrology* **50**, 1107–1148.

Elliott, T. (2003). Tracers of the slab. In: Eiler, J. M. (ed.) *Inside the Subduction Factory. American Geophysical Union, Geophysical Monograph* **138**, 23–45.

Ellis, D. J. (1986). Garnet–liquid Fe^{2+}–Mg equilibria and implications for the beginning of melting in the crust and subduction zones. *American Journal of Science* **286**, 765–791.

Ferrando, S., Frezzotti, M. L., Dallai, L. & Compagnoni, R. (2005). Fluid–rock interaction in UHP phengite–kyanite–epidote eclogite from the Sulu orogen, Eastern China. *International Geology Review* **47**, 750–775.

Fine, G. & Stolper, E. (1985). The speciation of carbon dioxide in sodium aluminosilicate glasses. *Contributions to Mineralogy and Petrology* **91**, 105–121.

Franck, S., Kossacki, K. & Bounama, C. (1999). Modelling the global carbon cycle for the past and future evolution of the Earth system. *Chemical Geology* **159**, 305–317.

Frei, D., Liebscher, A., Wittenberg, A. & Shaw, C. S. J. (2003). Crystal chemical controls on rare earth element partitioning between epidote-group minerals and melts: an experimental and theoretical study. *Contributions to Mineralogy and Petrology* **146**, 192–204.

Gorman, P. J., Kerrick, D. M. & Connolly, J. A. D. (2006). Modeling open system metamorphic decarbonation of subducting slabs. *Geochemistry, Geophysics, Geosystems* **7**, doi:10.1029/2005GC001125.

Grassi, D. & Schmidt, M. W. (2011*a*). Melting of carbonated pelites at 8–13 GPa: generating K-rich carbonatites for mantle metasomatism. *Contributions to Mineralogy and Petrology* **162**, 169–191.

Grassi, D. & Schmidt, M. W. (2011*b*). The melting of carbonated pelites from 70 to 700 km depth. *Journal of Petrology* **52**, 765–789.

Hacker, B. R., Rubie, D. C., Kirby, S. H. & Bohlen, S. R. (2005). The calcite–aragonite transformation in low-Mg marble: Equilibrium relations, transformation mechanisms, and rates. *Journal of Geophysical Research* **110**, B03205.

Hawkesworth, C. J., Gallagher, K., Hergt, J. M. & McDermott, F. (1993). Mantle and slab contributions in arc magmas. *Annual Review of Earth and Planetary Sciences* **21**, 175–204.

Hayes, D. E., Pimm, A. C., Beckmann, J. P., Benson, W. E., Berger, W. H., Roth, P. H., Supko, P. R. & von Rad, U. (1972). Part I: Shipboard site reports: Sites 143–144. *Initial reports of the Deep Sea Drilling Project Volume* **XIV**, 283–338.

Hayes, J. M. & Waldbauer, J. R. (2006). The carbon cycle and associated redox processes through time. *Philosophical Transactions of the Royal Society of London, Series B* **361**, 931–950.

Hazen, R. M., Hemley, J. R. & Mangum, A. J. (2012). Carbon in Earth's interior, storage, cycling and life. *EOS Transactions, American Geophysical Union* **93**, 17–28.

Hermann, J. (2002). Experimental constraints on phase relations in subducted continental crust. *Contributions to Mineralogy and Petrology* **143**, 219–235.

Hermann, J. & Rubatto, D. (2009). Accessory phase control on the trace element signature of sediment melts in subduction zones. *Chemical Geology* **265**, 512–526.

Hermann, J. & Spandler, C. J. (2008). Sediment melts at sub-arc depths: An experimental study. *Journal of Petrology* **49**, 717–740.

Hermann, J., Spandler, C., Hack, A. & Korsakov, A. V. (2006). Aqueous fluids and hydrous melts in high-pressure and ultra-high pressure rocks: implications for element transfer in subduction zones. *Lithos* **92**, 399–417.

Hernlund, J., Leinenweber, K., Locke, D. & Tyburczy, J. A. (2006). A numerical model for steady-state temperature distributions in solid-medium high-pressure cell assemblies. *American Mineralogist* **91**, 295–305.

Holdaway, M. J. (1972). Thermal stability of Al–Fe epidote as a function of fO_2 and Fe content. *Contributions to Mineralogy and Petrology* **37**, 307–340.

Holland, T. J. B. & Powell, R. (1998). An internally-consistent thermodynamic dataset for phases of petrological interest. *Journal of Metamorphic Geology* **16**, 309–344.

Irving, A. J. & Wyllie, P. J. (1975). Subsolidus and melting relationships for calcite, magnesite and the join $CaCO_3$–$MgCO_3$ to 36 kbar. *Geochimica et Cosmochimica Acta* **39**, 35–53.

Javoy, M., Pineau, F. & Allègre, C. J. (1982). Carbon geodynamical cycle. *Nature* **300**, 171–173.

Jochum, K. P., Dingwell, D. B., Rocholl, A., et al. (2000). The preparation and preliminary characterisation of eight geological MPI-DING reference glasses for *in-situ* microanalysis. *Geostandards Newsletter* **24**, 87–133.

John, T., Schenk, V., Mezger, K. & Tembo, F. (2004). Timing and *P–T* evolution of whiteschist metamorphism in the Lufilian Arc–Zambezi Belt orogen (Zambia): implications to the Gondwana assembly. *Journal of Geology* **112**, 71–90.

John, T., Klemd, R., Gao, J. & Garbe-Schönberg, C.-D. (2008). Trace-element mobilization in slabs due to non steady-state fluid–rock interaction: constraints from an eclogite-facies transport vein in blueschist (Tianshan, China). *Lithos* **103**, 1–24.

Johnson, M. C. & Plank, T. (1999). Dehydration and melting experiments constrain the fate of subducted sediments. *Geochemistry, Geophysics, Geosystems* **1**, 1999GC000014.

Kadik, A. & Lebedev, Y. (1968). Temperature dependence of the solubility of water in an albite melt at high pressures. *Geochemistry International* **5**, 1172–1181.

Kägi, R., Müntener, O., Ulmer, P. & Ottolini, L. (2005). Piston-cylinder experiments on H_2O undersaturated Fe-bearing systems: An experimental setup approaching fO_2 conditions of natural calc-alkaline magmas. *American Mineralogist* **90**, 708–717.

Keppler, H. (1989). The influence of the fluid phase composition on the solidus temperatures in the haplogranite system $NaAlSi_3O_8$–$KAlSi_3O_8$–SiO_2–H_2O–CO_2. *Contributions to Mineralogy and Petrology* **102**, 321–327.

Kerrick, D. M. & Connolly, J. A. D. (1998). Subduction of ophicarbonates and recycling of CO_2 and H_2O. *Geology* **26**, 375–378.

Kerrick, D. M. & Connolly, J. A. D. (2001a). Metamorphic devolatilization of subducted mid-ocean ridge metabasalts: implications for seismicity, arc magmatism and volatile recycling. *Earth and Planetary Science Letters* **189**, 19–29.

Kerrick, D. M. & Connolly, J. A. D. (2001b). Metamorphic devolatilization of subducted marine sediments and the transport of volatiles into the Earth's mantle. *Nature* **411**, 293–296.

Kessel, R., Ulmer, P., Pettke, T., Schmidt, M. W. & Thompson, A. B. (2005). The water–basalt system at 4 to 6 GPa: Phase relations and second critical endpoint in a K-free eclogite at 700 to 1400°C. *Earth and Planetary Science Letters* **237**, 873–892.

King, P. L. & Holloway, J. R. (2002). CO_2 solubility and speciation in intermediate (andesitic) melts: the role of H_2O and composition. *Geochimica et Cosmochimica Acta* **66**, 1627–1640.

Kjarsgaard, B. A. (1998). Phase relations of a carbonated high-CaO nephelinite at 0·2 and 0·5 GPa. *Journal of Petrology* **39**, 2061–2075.

Klemme, S., Blundy, J. D. & Wood, B. J. (2002). Experimental constraints on major and trace element partitioning during partial melting of eclogite. *Geochimica et Cosmochimica Acta* **66**, 3109–3123.

Klimm, K., Bundy, J. D. & Green, T. H. (2008). Trace element partitioning and accessory phase saturation during H_2O-saturated melting of basalt with implications for subduction zone chemical fluxes. *Journal of Petrology* **49**, 523–553.

Lecuyer, C. & Ricard, Y. (1999). Long-term fluxes of ferric iron: implication on the redox state of Earth mantle. *Earth and Planetary Science Letters* **165**, 197–211.

Liou, J. G. (1973). Synthesis and stability relations of epidote, $Ca_2Al_2FeSi_3O_{12}(OH)$. *Journal of Petrology* **14**, 381–413.

Liou, J. G., Kim, H. S. & Maruyama, S. (1983). Prehnite–epidote equilibria and their petrologic applications. *Journal of Petrology* **24**, 321–342.

Mann, U. & Schmidt, M. W. (in press). Melting of pelitic sediments at subarc depths: 1. Flux vs. fluid-absent melting and a parameterization of melt productivity. *Chemical Geology*. http://dx.doi.org/10.1016/j.chemgeo.2015.02.032

Manning, C. E. (2004). The chemistry of subduction-zone fluids. *Earth and Planetary Science Letters* **223**, 1–16.

Manning, C. E., Shock, E. L. & Sverjensky, D. A. (2013). The chemistry of carbon in aqueous fluids at crustal and upper-mantle conditions: experimental and theoretical constraints. In: Hazen, R. M., Jones, A. P. & Baross, J. A. (eds) *Carbon in Earth. Mineralogical Society of America and Geochemical Society, Reviews in Mineralogy and Geochemistry* **75**, 109–148.

Martin, L. A. J., Wood, B. J., Turner, S. & Rushmer, T. (2011). Experimental measurements of trace element partitioning between lawsonite, zoisite and fluid and their implication for the composition of arc magmas. *Journal of Petrology* **52**, 1049–1075.

Martin, L. H. J., Schmidt, M. W., Mattsson, H. B. & Günther, D. (2013). Element partitioning between immiscible carbonatite and silicate melts for dry and H_2O-bearing systems at 1–3 GPa. *Journal of Petrology* **54**, 2301–2338.

Martindale, M., Skora, S., Pickles, J., Elliott, T., Bundy, J. & Avanzinelli, R. (2013). High pressure phase relations of subducted volcaniclastic sediments from the West Pacific and their implications for the geochemistry of the Marianas arc magmas. *Chemical Geology* **342**, 94–109.

Marty, B. & Jambon, A. (1987). $C/^3He$ fluxes in volatile fluxes from the solid Earth: implications for carbon geodynamics. *Earth and Planetary Science Letters* **83**, 16–26.

McCulloch, M. T. & Gamble, J. A. (1991). Geochemical and geodynamical constraints on subduction zone magmatism. *Earth and Planetary Science Letters* **102**, 358–374.

McDade, P., Wood, B., Van Westrenen, W., Brooker, R., Gudmundsson, G., Soulard, H., Najorka, J. & Blundy, J. (2002). Pressure corrections for a selection of piston-cylinder assemblies. *Mineralogical Magazine* **66**, 1021–1028.

McDermott, F. & Hawkesworth, C. (1991). Th, Pb, and Sr isotope variations in young island arc volcanics and oceanic sediments. *Earth and Planetary Science Letters* **104**, 1–15.

McMillan, P. F. & Holloway, J. R. (1987). Water solubility in aluminosilicate melts. *Contributions to Mineralogy and Petrology* **97**, 320–332.

Molina, J. F. & Poli, S. (2000). Carbonate stability and fluid composition in subducted oceanic crust: an experimental study on H_2O–CO_2-bearing basalts. *Earth and Planetary Science Letters* **176**, 295–310.

Mysen, B. O. (1976). The role of volatiles in silicate melts: solubility of carbon dioxide and water in feldspar, pyroxene, feldspathoid melts to 30 kb and 1625 degrees C. *American Journal of Science* **276**, 969–996.

Nichols, G. T., Wyllie, P. J. & Stern, C. R. (1994). Subduction-zone melting of pelagic sediments constrained by melting experiments. *Nature* **371**, 785–788.

Nichols, G. T., Wyllie, P. J. & Stern, C. R. (1996). Experimental melting of pelagic sediment, constraints relevant to subduction. In: Bebout, G. E., Scholl, D. H., Kirby, S. P. & Platt, J. (eds) *Subduction: Top to Bottom. American Geophysical Union, Geophysical Monograph* **96**, 293–298.

Nishio, Y., Sasaki, S., Gamo, T., Hiyagon, H. & Sano, Y. (1998). Carbon and helium isotope systematics of North Fiji Basin basalt glasses: carbon geochemical cycle in the subduction zone. *Earth and Planetary Science Letters* **154**, 127–138.

Paillat, O., Elphick, S. C. & Brown, W. L. (1992). The solubility of water in $NaAlSi_3O_8$ melts: a re-examination of Ab–H_2O phase relationships and critical behaviour at high pressures. *Contributions to Mineralogy and Petrology* **112**, 490–500.

Pearce, J. A. & Cann, J. R. (1973). Tectonic setting of basic volcanic rocks determined using trace-element analyses. *Earth and Planetary Science Letters* **19**, 290–300.

Plank, T. & Langmuir, C. H. (1998). The chemical composition of subducting sediment and its consequences for the crust and mantle. *Chemical Geology* **145**, 325–394.

Poli, S. & Schmidt, M. W. (2002). Petrology of subducted slabs. *Annual Review of Earth and Planetary Sciences* **30**, 207–235.

Poli, S., Franzolin, E., Fumagalli, P. & Crottini, A. (2009). The transport of carbon and hydrogen in subducted oceanic crust: An experimental study to 5 GPa. *Earth and Planetary Science Letters* **278**, 350–360.

Prouteau, G. & Scaillet, B. (2013). Experimental constraints on sulphur behaviour in subduction zones:

implications for TTG and adakite production and the global sulphur cycle since the Archean. *Journal of Petrology* **54**, 183–213.

Proyer, A., Rolfo, F., Castelli, D. & Compagnoni, R. (2014). Diffusion-controlled metamorphic reaction textures in an ultrahigh-pressure impure calcite marble from Dabie Shan, China. *European Journal of Mineralogy* **26**, 25–40.

Rea, D. K. & Ruff, L. J. (1996). Composition and mass flux of sediment entering the world's subduction zones: Implications for global sediment budgets, great earthquakes, and volcanism. *Earth and Planetary Science Letters* **140**, 1–12.

Reinecke, T. (1998). Prograde high- to ultrahigh-pressure metamorphism and exhumation of oceanic sediments at Lago di Cignana, Zermatt–Saas Zone, western Alps. *Lithos* **42**, 147–189.

Rohrbach, A. & Schmidt, M. W. (2011). Redox freezing and melting in the Earth's deep mantle resulting from carbon–iron redox coupling. *Nature* **472**, 209–212.

Rolfo, F., Compagnoni, R., Wu, W. & Xu, S. (2004). A coherent lithostratigraphic unit in the coesite–eclogite complex of Dabie Shan, China: geologic and petrologic evidence. *Lithos* **73**, 71–94.

Rubatto, D. & Hermann, J. (2007). Experimental zircon/melt and zircon/garnet trace element partitioning and implications for the geochronology of crustal rocks. *Chemical Geology* **241**, 38–61.

Sano, Y. & Marty, B. (1995). Origin of carbon in fumarolic gas from island arcs. *Chemical Geology* **119**, 265–274.

Sano, Y. & Williams, S. N. (1996). Fluxes of mantle and subducted carbon along convergent plate boundaries. *Geophysical Research Letters* **23**, 2749–2752.

Schmidt, M. W. & Poli, S. (1998). Experimentally based water budgets for dehydrating slabs and consequences for arc magma generation. *Earth and Planetary Science Letters* **163**, 361–379.

Schmidt, M. W. & Ulmer, P. (2004). A rocking multianvil: elimination of chemical segregation in fluid-saturated high-pressure experiments. *Geochimica et Cosmochimica Acta* **68**, 1889–1899.

Schmidt, M. W., Vielzeuf, D. & Auzanneau, E. (2004). Melting and dissolution of subducting crust at high pressures: the key role of white mica. *Earth and Planetary Science Letters* **228**, 65–84.

Shaw, A. M., Hilton, D. R., Fischer, T. P., Walker, J. A. & Alvarado G. E. (2003). Contrasting He–C relationships in Nicaragua and Costa Rica: insights into C cycling through subduction zones. *Earth and Planetary Science Letters* **214**, 499–513.

Skora, S. & Blundy, J. (2010). High-pressure hydrous phase relations of radiolarian clay and implications for the involvement of subducted sediment in arc magmatism. *Journal of Petrology* **51**, 2211–2243.

Skora, S. & Blundy, J. (2012). Monazite solubility in hydrous silicic melts at high pressure conditions relevant to subduction zone metamorphism. *Earth and Planetary Science Letters* **321–322**, 104–114.

Sleep, N. H. & Zahnle, K. (2001). Carbon dioxide cycling and implications for climate on ancient Earth. *Journal of Geophysical Research* **106**, 1373–1399.

Sorensen, S. S., Grossman, J. N. & Perfit, M. R. (1997). Phengite-hosted LILE enrichment in eclogite and related rocks; implications for fluid-mediated mass transfer in subduction zones and arc magma genesis. *Journal of Petrology* **38**, 3–34.

Spandler, C., Hermann, J., Arculus, R. & Mavrogenes, J. (2003). Redistribution of trace elements during prograde metamorphism from lawsonite blueschist to eclogite facies; implications for deep subduction-zone processes. *Contributions to Mineralogy and Petrology* **146**, 205–222.

Spandler, C., Yaxley, G., Green, D. H. & Scott, D. (2010). Experimental phase and melting relations of metapelite in the upper mantle: implications for the petrogenesis of intraplate magmas. *Contributions to Mineralogy and Petrology* **160**, 569–589.

Spandler, C. J. & Pirard, C. (2013). Element recycling from subducting slabs to arc crust: a review. *Lithos* **170–171**, 208–223.

Stamper, C. C., Melekhova, E., Bundy, J. D., Arculus, R. J., Humphreys, M. C. S., Broker, R. A. (2014). Oxidised phase relations of a primitive basalt from Grenada, Lesser Antilles. *Contributions to Mineralogy and Petrology* **167**, doi:10.1007/s00410-013-0954-6.

Staudigel, H., Hart, S. R., Schmincke, H.-U. & Smith, B. M. (1989). Cretaceous ocean crust at DSDP Site 417 and Site 418—carbon uptake from weathering versus loss by magmatic outgassing. *Geochimica et Cosmochimica Acta* **53**, 3091–3094.

Suess, E. & Whiticar, M. J. (1989). Methane-derived CO_2 in pore fluids expelled from the Oregon subduction zone. *Palaeogeography, Palaeoclimatology, Palaeoecology*, **71** 119–136.

Syracuse, E. M., Van Keken, P. E. & Abers, G. A. (2010). The global range of subduction zone thermal models. *Physics of the Earth and Planetary Interiors* **183**, 73–90.

Terry, M. P., Robinson, P. & Krogh Ravna, E. J. (2000). Kyanite eclogite thermobarometry and evidence for thrusting of UHP over HP metamorphic rocks, Nordøyane, Western Gneiss Region, Norway. *American Mineralogist* **85**, 1637–1650.

Thirlwall, M. F., Smith, T. E., Graham, A. M., Theodorou, N., Hollings, P., Davidson, J. P. & Arculus, R. J. (1994). High-field strength element anomalies in arc lavas—source or process. *Journal of Petrology* **35**, 819–838.

Thomsen, T. B. & Schmidt, M. W. (2008a). Melting of carbonated pelites at 2·5–5·0 GPa, silicate–carbonatite liquid immiscibility, and potassium–carbon metasomatism of the mantle. *Earth and Planetary Science Letters* **267**, 17–31.

Thomsen, T. B. & Schmidt, M. W. (2008b). The biotite to phengite reaction and mica-dominated melting in fluid + carbonate-saturated pelites at high pressures. *Journal of Petrology* **49**, 1889–1914.

Truckenbrodt, J., Ziegenbein, D. & Johannes, W. (1997). Redox conditions in piston cylinder apparatus: The different behavior of boron nitride and unfired pyrophyllite assemblies. *American Mineralogist* **82**, 337–344.

Tsuno, K. & Dasgupta, R. (2011). Melting phase relation of nominally anhydrous, carbonated pelitic-eclogite at 2·5–3·0 GPa and deep cycling of sedimentary carbon. *Contributions to Mineralogy and Petrology* **161**, 743–763.

Tsuno, K. & Dasgupta, R. (2012). The effect of carbonates on near-solidus melting of pelite at 3 GPa: relative efficiency of H_2O and CO_2 subduction. *Earth and Planetary Science Letters* **319–320**, 185–196.

Tsuno, K., Dasgupta, R., Danielson, L. & Righter, K. (2012). Flux of carbonate melt from deeply subducted pelitic sediments—geophysical and geochemical implications for the source of Central American volcanic arc. *Geophysical Research Letters* **39**, L16307.

Ulmer, P. & Trommsdorff, V. (1995). Serpentine stability to mantle depths and subduction-related magmatism. *Science* **268**, 858–861.

van Keken, P. E., Kiefer, B. & Peacock, S. M. (2002). High-resolution models of subduction zones: implications for

mineral dehydration reactions and the transport of water into the deep mantle. *Geochemistry, Geophysics, Geosystems* **3**, doi:10.1029/2001GC000256.

Van Keken, P. E., Hacker, B. R., Syracuse, E. M. & Abers, G. A. (2011). Subduction factory: 4. Depth-dependent flux of H2O from subducting slabs worldwide. *Journal of Geophysical Research* **116**, B01401, 1–15.

Van Soest, M. C., Hilton, D. R. & Kreulen, R. (1998). Tracing crustal and slab contributions to arc magmatism in the Lesser Antilles island arc using helium and carbon relationships in geothermal fluids. *Geochimica et Cosmochimica Acta* **62**, 3323–3335.

Walter, M. J., Kohn, S. C., Araujo, D., Bulanova, G. P., Smith, C. B., Gaillou, E., Wang, J., Steele, A. & Shirey, S. B. (2011). Deep mantle cycling of oceanic crust: evidence from diamonds and their mineral inclusions. *Science* **334**, 54–57.

Wei, C., Wang, W., Clarke, G. L., Zhang, L. & Song, S. (2009). Metamorphism of high/ultrahigh-pressure pelitic–felsic schist in the South Tianshan Orogen, NW China: phase equilibria and *P–T* path. *Journal of Petrology* **50**, 1973–1991.

Wilson, A. (1960). The micro-determination of ferrous iron in silicate minerals by a volumetric and colorimetric method. *Analyst* **85**, 823–827.

Yaxley, G. M. & Green, D. H. (1994). Experimental demonstration of refractory carbonate-bearing eclogite and siliceous melt in the subduction regime. *Earth and Planetary Science Letters* **128**, 313–325.

Zhang, R. Y., Liou, J. G. & Ernst, W. G. (2009). The Dabie–Sulu continental collision zone: A comprehensive review. *Gondwana Research* **16**, 1–26.

Zheng, Y.-F., Fu, B., Gong, B. & Li, L. (2003). Stable isotope geochemistry of ultrahigh pressure metamorphic rocks from the Dabie–Sulu orogen in China: implications for geodynamics and fluid regime. *Earth-Science Reviews* **62**, 105–161.